Integrated Hydrological Modelling of Surface-groundwater Interactions in Hard Rock System of the Sardon Catchment (Spain) and Comparison with Selected Satellite Product

SHIXIAN XU

August, 2021

SUPERVISORS:
Dr. Maciek.W. Lubczynski
Dr. Yijian Zeng

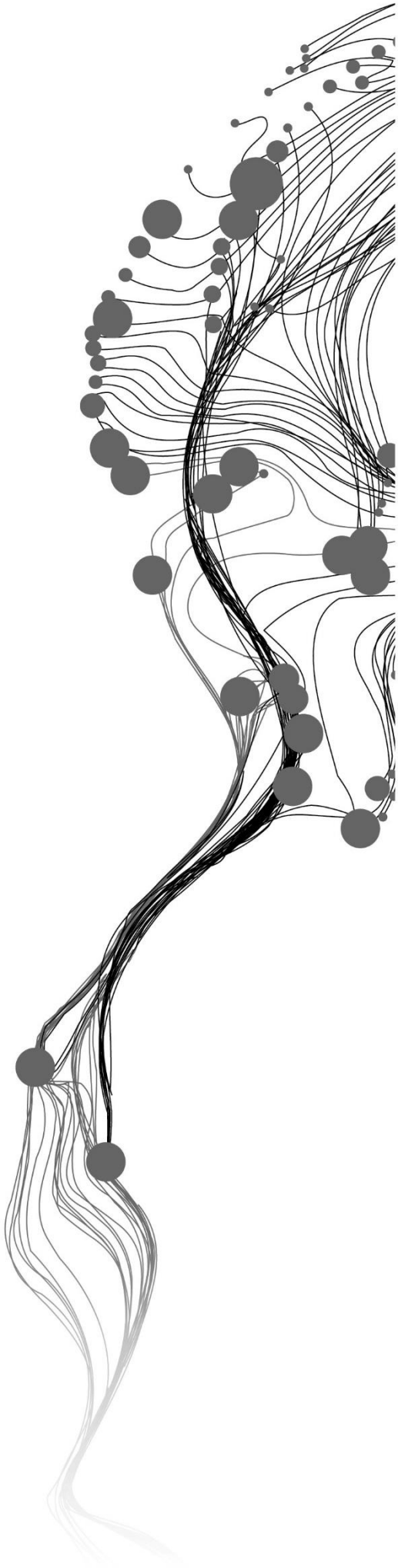

Integrated Hydrological Modelling of Surface-groundwater Interactions in Hard Rock System of the Sardon Catchment (Spain) and Comparison with Selected Satellite Product

SHIXIAN XU
Enschede, The Netherlands, August, 2021

Thesis submitted to the Faculty of Geo-Information Science and Earth Observation of the University of Twente in partial fulfilment of the requirements for the degree of Master of Science in Geo-information Science and Earth Observation.
Specialisation: Water Resources and Environmental Management

SUPERVISORS:
Dr. Maciek.W. Lubczynski
Dr. Yijian Zeng

THESIS ASSESSMENT BOARD:
Dr. Christiaan van der Tol (Chair)
Dr. Jacek Gurwin (External Examiner, University of Wroclaw, Poland)

ABSTRACT

Hard rock systems (HRSs) are widely spread over the world and known for relatively low groundwater productivity, but certain areas still heavily depend on groundwater in order to fulfil the need for irrigation and domestic water use, especially in a water-limited environment (WLE). HRSs are characterised by variable density of fault and fractures, shallow water table and low storativity. These characteristics lead to complex surface-groundwater interactions, therefore studying those such areas is critical for local groundwater management in sustainable manner. In this study, the selected study area, the Sardon catchment (Spain), represents typical HRS-WLE characteristics.

An integrated hydrological model (IHM) was built for the Sardon catchment based on MODFLOW 6, the latest version of MODFLOW. Efforts were made in three directions: i) apply remote sensing techniques for improving driving forces estimation; ii) calibrate the Sardon model involving MODIS ET, next to hydraulic heads, as calibration state variables to improve water balance and overall model reliability; iii) compare the simulated soil moisture with SSM1km product.

The Sardon model was calibrated in the transient state for 8 hydrological years (2009 ~ 2016) with daily groundwater heads and yearly MODIS ET. Even though the model was calibrated only by yearly MODIS ET (yearly difference within ±15%), the daily simulated ET showed surprisingly good match with daily MODIS ET (RMSE = 0.57mm).

Overall, the simulated soil moisture showed a good agreement with the SSM1km product (RMSE = 0.081 m^3 m^{-3} and Pearson correlation (r) = 0.65). Better agreement between simulated and satellite soil moisture was observed in dry days (RMSE = 0.057 m^3 m^{-3}, r = 0.69) than in rainy days (RMSE = 0.102 m^3 m^{-3}, r = 0.54).

The transient model simulation showed that 8-year mean gross groundwater recharge (R_g) was 23.1% of precipitation (P). Over 90% of R_g was lost out of the groundwater zone by groundwater exfiltration (Exf_{gw}) and groundwater evapotranspiration (ET_g). The groundwater net recharge (R_n) was highly spatial variable and temporally variable ranging from -28.17 mm yr^{-1} in dry year 2009 and 0.02 mm yr^{-1} in wet year 2010.

The MODFLOW 6 showed great ability in simulating surface-groundwater interactions in complex hydrogeological hard rock systems, such as Sardon catchment and in derivation of realistic water balances for both unsaturated and saturated zones.

Keywords: hard rock systems, water-limited environment, MODFLOW 6, surface-groundwater interactions, soil moisture

ACKNOWLEDGEMENTS

How time flies. The two-year journey is memorable.

I would like to express my sincere appreciation to my first supervisor, Dr. Maciek Lubczynski. Thanks for his patient guidance, encouragement and generous support along the way. I also would like to thank my second supervisor, Dr. Yijian Zeng, for his critical comments.

Special thanks to my advisor, Mostafa Gomma Daoud. I am grateful for all the discussions and technical help for data processing. All the best to the PhD journey.

Sincerely thanks to Ir. Arno van Lieshout, the specialisation coordinator and my mentor. Thanks for his concerns, advice and efforts for holding recreational events during the Covid period.

Sincerely thanks to all the teaching staffs of the Water Resource Department: Prof. Su, Dr. Christiaan van der Tol, Dr. Chris Mannaerts, Dr. Suhyb Salama, Dr. Rogier van der Velde, Dr. Zoltan Vekerdy, Dr. Wim Timmermans, Dr. Tom Rientjes, Dr. Ben Maathuis, Ir. Gabriel Parodi, Ir. Harm-jan Benninga. Thanks for offering me the excellent specialisation course at ITC.

Deeply thanks to the two ladies from the Student Affairs, Marie-Chantal Metz-Bekkers and Theresa van den Boogaard. I am very grateful for all the support and encouragement during the tough period. It made me feel like home.

Sincerely thanks to all my classmates and friends. It is a precious experience to meet all of you in Enschede.

Finally, I would like to thank my family for their love and support, which encourages me to pursue the MSc degree.

TABLE OF CONTENTS

LIST OF FIGURES

LIST OF TABLES

1. INTRODUCTION

1.1. General background

Groundwater is an important source for freshwater supply. Thirty per cent of the world's freshwater is contributed by groundwater, compared with 68.7% for Glaciers and ice caps and 1.2% for surface and other freshwater sources (Peter H. Gleick, 1993). Excluding glacier and ice caps, groundwater represents 98.5% of total water resources of the Earth (Hiscock, 2005).

Groundwater is an essential part for human society. Because of the complex recharge processes, groundwater is less vulnerable to pollution than surface water. Also, the structure of aquifers allows groundwater to be stored in the long-term preventing it from evapotranspiration. Due to these reasons, groundwater is advantageous for freshwater supply, for instance, drinking water, irrigation, domestic use, industrial use and so on. The high dependency on groundwater leads to intensive pumping, and sometimes over-abstraction may happen in unsustainable way. Groundwater is naturally replenished, although recharge rate could be insufficient. Therefore, from a long-term perspective, it is necessary to understand the dynamics of groundwater systems and surface-groundwater interactions for sustainable water resources management, especially in water-limited environments.

Water-limited environments (WLEs) are the areas with aridity condition, and the characteristic of WLEs is that the annual precipitation (P) is typically less than annual potential evapotranspiration (PET) (Newman et al., 2006). In order to evaluate the aridity condition, the United Nations Environment Programme (UNEP) introduced the Aridity Index (AI), which is calculated by dividing P by PET (UNEP, 1997). According to the value of AI, WLEs can be categorized as hyper-arid ($AI < 0.05$), arid ($0.05 < AI < 0.2$), semi-arid ($0.2 < AI < 0.5$) and sub-humid ($0.5 < AI < 0.65$) regions. Due to the relatively low ratio of P and PET, groundwater could be the primary water resource in the WLEs. In this case, understanding the local groundwater system is important.

Hard rock systems (HRSs) are widely spread over the world and account for about 20 per cent of the land surface (Singhal, 2008). From the geological perspective, HRSs are composed of crystalline rocks, including plutonic and morphic rocks (Lachassagne et al., 2011). Even though the HRSs are known for relatively low groundwater productivity, certain areas may still heavily depend on groundwater in order to fulfil the need for irrigation and domestic water use (Ebrahim et al., 2019). Because of the complex structure of HRSs, it is challenging to understand the dynamics of surface-groundwater interactions in these regions, but it is critical for sustainable groundwater management. In HRSs, water moves through secondary porosity consisting of fractures, joints and faults. One of the characteristics of HRSs is relatively low storativity, and this could result in typical occurrence of shallow water table and related, dramatic seasonal land cover changes in such areas. For example, during the wet season, a land cover could be having widespread water bodies and grasses, while during the dry season, it could covert to an extensive occurrence of bare lands. The seasonal changes in the land cover imply complex surface-groundwater interactions, particularly distinct in HRS-WLE.

The selected study area for this research, i.e., Sardon catchment, represents typical HRS-WLE characteristics.

1.2. Previous work

In the Sardon catchment, many research studies have been carried out. Even though those studies differ in directions, data used, partitioning of evapotranspiration, way of assessment of rainfall interception, conceptual model definition, type and scale of a numerical model, they all contribute to a better understanding of the water cycle at the Sardon catchment.

For understanding the dynamics of the groundwater system, the numerical modelling of groundwater is a powerful approach, especially in the geologically complex HRSs. Numerical models are capable of solving transient, 3D, heterogeneous and anisotropic governing equation under complex boundary and initial conditions (Anderson et al., 2015). One of the most well-known numerical codes for groundwater modelling is called MODFLOW (McDonald and Harbaugh, 1988). It has been applied and kept updating for the last decades. Compared with the traditional standalone groundwater model applying externally calculated recharge as the input, recent integrated hydrological model (IHM) is more advantageous for simulating surface-groundwater interaction because IHM is capable of internally simulating exchange processes between surface, unsaturated zone and saturated zone (Huntington and Niswonger, 2012). In sardon catchment, studies were carried out by applying standalone groundwater model and IHM, respectively.

Lubczynski and Gurwin (2005) integrated various data sources and methods for transient groundwater modelling in Sardon catchment. Even though the standalone groundwater model was used, they applied RS-GIS technique to determine the spatial distribution pattern of hydrogeological parameters (hydraulic conductivity and storage coefficient) and the spatio-temporal pattern of essential fluxes (evapotranspiration and recharge). Besides, they pointed out that groundwater evaporation (E_g) in the study area has a large contribution in groundwater balance because of the shallow groundwater table and low retention capacity of the fractured unsaturated zone. The approach of combining RS-GIS technique and standalone groundwater model provided an opportunity to understand the hydrologically and structurally complex HRS at that time. Later, with the model improvement, the new model considering the surface, unsaturated and saturated zones emerged.

Hassan et al. (2014) used Groundwater and Surface water Flow (GSFLOW) to study the effect of surface-groundwater interaction in the Sardon catchment. GSFLOW is an integrated hydrological model and is formed by the integration of Precipitation Runoff Modeling System (PRMS) and MODFLOW (Markstrom et al., 2008). In their study, PRMS simulated the surface and soil zones, and it was linked to MODFLOW-NWT (Niswonger et al., 2011) by Unsaturated Zone Flow (UZF1) Package (Niswonger and Prudic, 2006) and Stream Flow Routing (SFR2) Package (Niswonger and Prudic, 2005). In such a modelling setup, complex and complete water balance can be calculated, including various runoff components and groundwater exfiltration. This is important for Sardon catchment because shallow water table and low storage of aquifers can result in rapid water table rise after a rainfall event. Even though the same conceptual model was used by Hassan et al. (2014) as by Lubczynski & Gurwin (2005), who used the standalone MODFLOW solution, the GSFLOW solution provided quite different results. For example, in Lubczynski & Gurwin (2005), groundwater evapotranspiration accounted for 36% of groundwater recharge (R_g), and the remaining 64% was attributed to groundwater outflow while in Hassan et al.

(2014), groundwater outflow only accounted for 5% of R_g . Besides, while the portion of groundwater evapotranspiration was similar (30% of R_g), in Hassan et al. (2014), surprisingly groundwater exfiltration took up 69% of R_g , the option not available in standalone groundwater models. This difference indicated the necessity of using integrated hydrological modelling approach for understanding complex dynamics of surface-groundwater interaction in HRSs.

An appropriate conceptual model is very important, especially for HRSs with structural and hydrogeological complexity, because it helps to understand the behaviour of a hydrogeological system and to support quantitative modelling. Francés et al. (2014) developed a new conceptual model for Sardon catchment by combining remote sensing, non-invasive hydrogeophysics and hydrogeological field data acquisition. With this multi-techniques methodology, they defined the catchment as two layers (saprolite and fissured layers) and six zones according to the distribution of faults. Besides, for each zone, they determined the geometry and the range of aquifer parameters (hydraulic conductivity, transmissivity, specific yield and storativity). These are valuable for future model setup.

Besides, there were three studies focusing on three aspects, i.e. tree transpiration, tree interception and bare soil evaporation. Reyes-Acosta and Lubczynski (2013) proposed a scaling-up method for quantifying dry-season tree transpiration of the Sardon catchment. This method is based on remote sensing and sap flow measurements. The obtained tree transpiration map helped to understand the spatial pattern of plant-water interaction in the dry season. Hassan et al. (2017) estimated the tree interception loss regarding the only two oak species (*Quercus ilex* and *Quercus pyrenaica*) in the Sardon catchment. They combined in-situ measurements (rainfall, throughfall and stemflow), Gash model temporal extrapolation and remote-sensing spatial upscaling. Balugani (2021) studied the separation of unsaturated zone evaporation (E_u) and groundwater evaporation (E_g) from soil evaporation (E_{ss}) in the semi-arid Sardon catchment. Substantial underestimation of E_{ss} and particularly E_g by commonly applied models was proved by proposed theoretical and experimental frameworks.

Daoud (2020) applied MODFLOW 6, the latest version of MODFLOW, with a novel unstructured grid approach (Voronoi grid) to simulate the unsaturated and saturated zones of Sardon catchment. In his study, a novel re-infiltration concept was introduced. Following that concept, the rejected infiltration and/or groundwater exfiltration, by applying the Water Mover (MVR) Package (Langevin et al., 2017), can be: i) routed as surface runoff to either downslope neighbouring UZF cells or the stream reaches defined by SFR package; ii) evapotranspired; or iii) re-infiltrated. The re-infiltration was not available in any of MODFLOW versions, so that concept improves the water balanced and reliability of the model simulation. In addition, Daoud (2020) estimated both interception and evapotranspiration of a grass, which was not taken into account in previous Sardon studies. The modelling results revealed the reliability of the unstructured grid approach, the importance of reinfiltration and the effectiveness of the integrated hydrological model (IHM) to simulate surface-groundwater interaction.

1.3. Research problem

Previous works have shown valuable insights into the geologically complex Sardon catchment representing typical HRS-WLE characteristics, but there are still some directions to be investigated as the following:

- Evapotranspiration is an important flux in the semi-arid Sardon catchment, but previous groundwater modelling practices did not consider actual evapotranspiration (ET_a) as a state variable for model calibration. To include ET_a for calibration is expected to constrain the model behaviour, and this approach may lead to a more representative water balance.
- Interception and potential evapotranspiration (PET) are two critical driving forces as inputs for the model, and there is a need to improve temporal estimation. While Daoud (2020) improved the estimation of interception and PET by considering the influence of grass, but he only evaluated monthly canopy storage capacity and crop coefficient for one year and assumed that these values are applicable for all other years of the simulation period. More representative driving forces are expected if the temporal variability can be improved. Eventually, water balance can be enhanced.
- MODFLOW 6, the latest version of MODFLOW, allows extracting simulated soil moisture in user-defined depth. It would be interesting to compare the satellite soil moisture with the soil moisture simulated and extracted from a well-calibrated model.

1.4. Research objectives

The main objective is to study the surface-groundwater interaction dynamics in the Sardon catchment.

Sub-objectives:

- Improve estimation of grass interception.
- Improve estimation of PET.
- Use ET_a for model calibration.
- Present long-term water balance.
- Compare the MODFLOW 6-simulated soil moisture with the Sentinel-1 satellite soil moisture.

1.5. Research questions

- How to improve grass interception estimation?
- How to improve PET estimation?
- How to use ET_a for calibration?
- How big is the difference between the MODFLOW6-simulated soil moisture and the Sentinel-1 satellite soil moisture?

2. STUDY AREA

2.1. Location and topography

The Sardon catchment (~ 80 km²) is located about 40 km northwest of Salamanca city, Spain (between 41°01' and 41°09' N, and 6°06' and 6°14' W). The terrain is undulating, and the elevation decreases from the catchment boundaries (E, S and W) towards the central Sardon river ranging between 870 m a.s.l. at the S boundary to 730 m a.s.l. at the northern Sardon river outlet. The catchment boundaries are characterised by rock outcrops. There are impermeable schists and massive granites at the southern boundary, massive granites at the western and northern boundaries, and fractured rocks filled with quartzite material at the eastern boundary (Lubczynski and Gurwin, 2005).

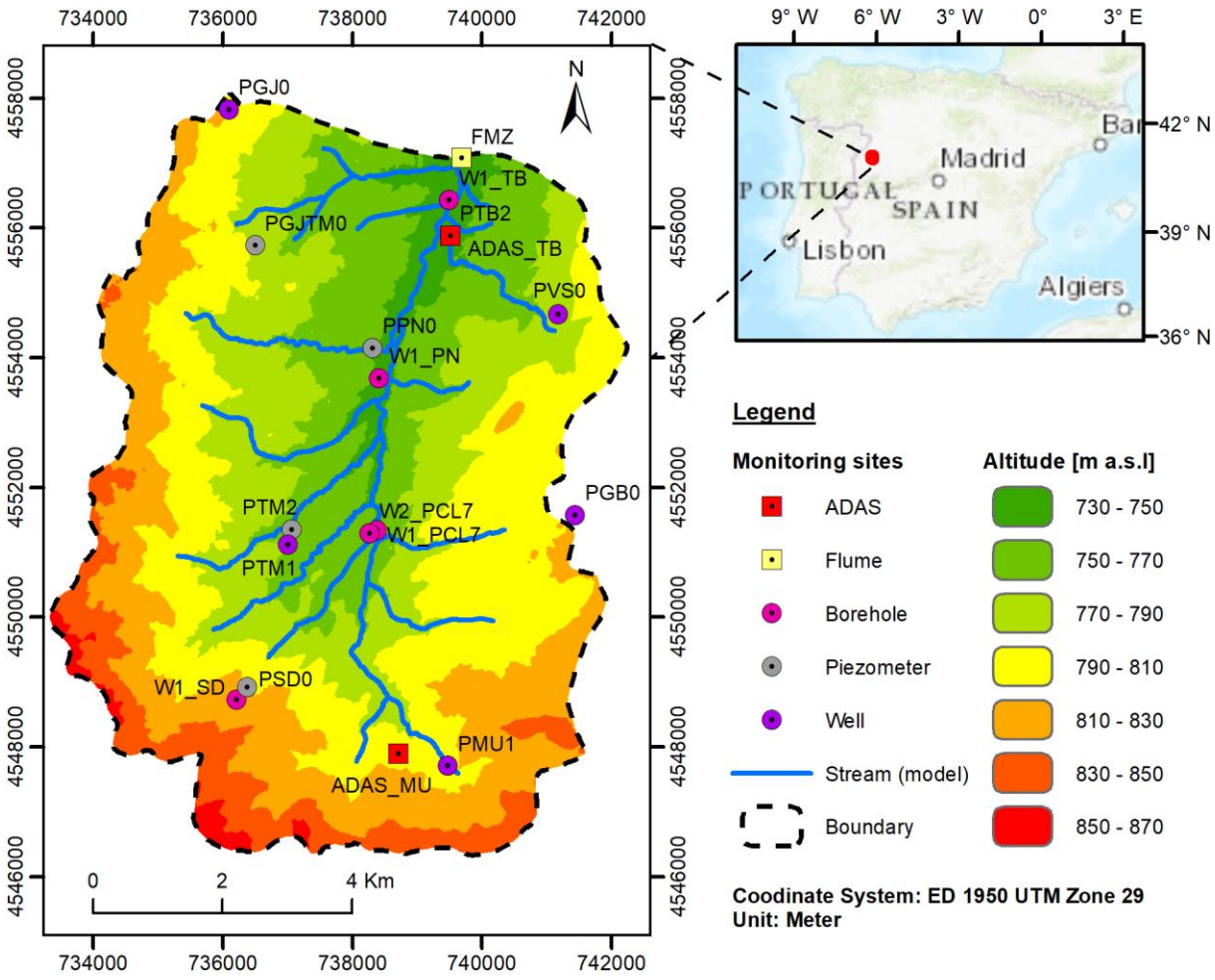

Figure 2.1 Map of the Sardon catchment and monitoring sites

2.2. Climate

The climate in the Sardon catchment is semi-arid, Mediterranean, typical for the central Iberian Peninsula. The long-term mean precipitation (1951~2012) is 586 mm y^{-1} with a standard deviation of 179 mm yr^{-1} (Hassan et al., 2014). The seasonal distribution of precipitation leads to the distinct dry seasons, from June to September and wet seasons, from October to May, with nearly annual precipitation. The warmest and driest months are July and August with a mean temperature of 22 °C, mean potential evapotranspiration (PET) of 5 mm day^{-1} and mean precipitation less than 20 mm mth^{-1}, while the coldest months are January and February with a mean temperature of 5 °C. The wettest months are October and November, with mean precipitation higher than 70 mm mth^{-1}, while the lowest PET occurs in December and January, on average 0.5 $mm.day^{-1}$ (Lubczynski and Gurwin, 2005).

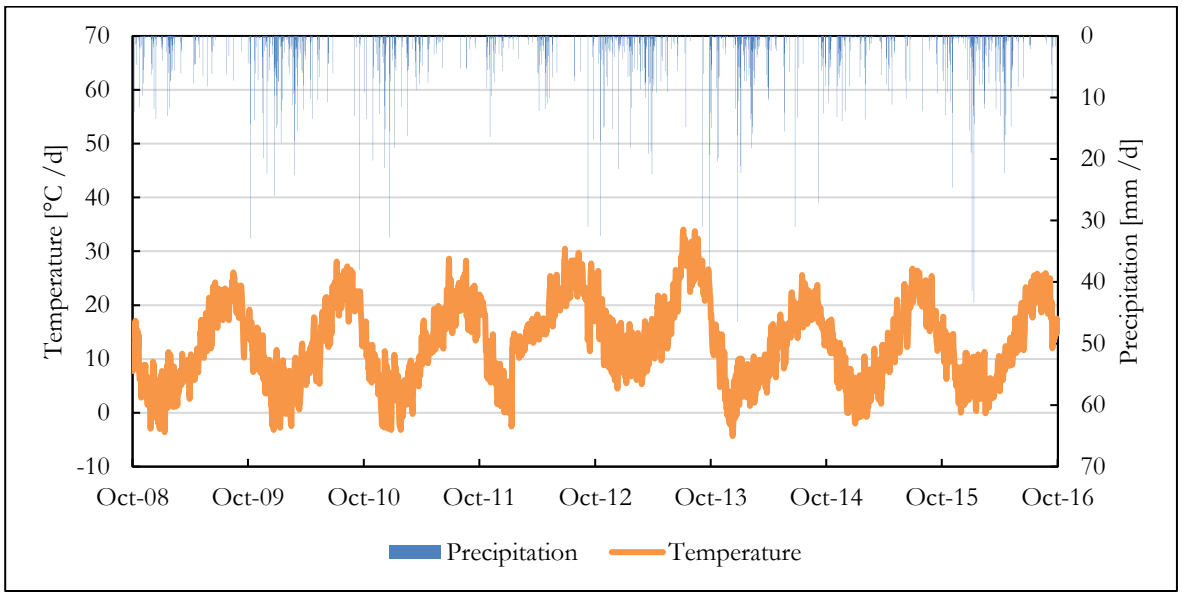

Figure 2.2 Daily precipitation and temperature in the Sardon catchment from 1 October 2008 to 30 September 2016 (eight hydrological years starting in Spain on 1 October and ending on 30 September).

2.3. Land cover

The Sardon catchment is typical oak savannah (also known as dehesa in Spain), and it is mainly used for pasture because of low fertility in the soil (Hassan et al., 2014). There are two types of oak trees, i.e. evergreen oak (*Quercus ilex)* and broad-leaf deciduous oak *(Quercus pyrenaica)*. These trees are sparsely distributed, covering around 7% of the study area (Reyes-Acosta and Lubczynski, 2013). The rest of the study area is dominated by seasonal grass, which is only green from early spring to early summer (March to May or June), successively consumed by the livestock, so from July, it is generally bare soil for the rest of the year (Balugani, 2021). Besides, next to trees, grasses and bare soil coverages, outcrops typical for HRS are present, as shown in Figure 2.3.

Francés et al. (2014) mapped the granite outcrops by using two high-resolution, multispectral satellite images (QuickBird from September 2009 and WorldView-2 from December 2012). Also, Reyes-Acosta and Lubczynski (2013) classified the two oak tree species with 90% overall accuracy with two high-resolution multispectral satellite images (QuickBird from August 2009 and WorldView-2 from December 2010). By combining these two maps, Gomaa (2020) classified six land cover types, and that land cover classification map is applied in this study.

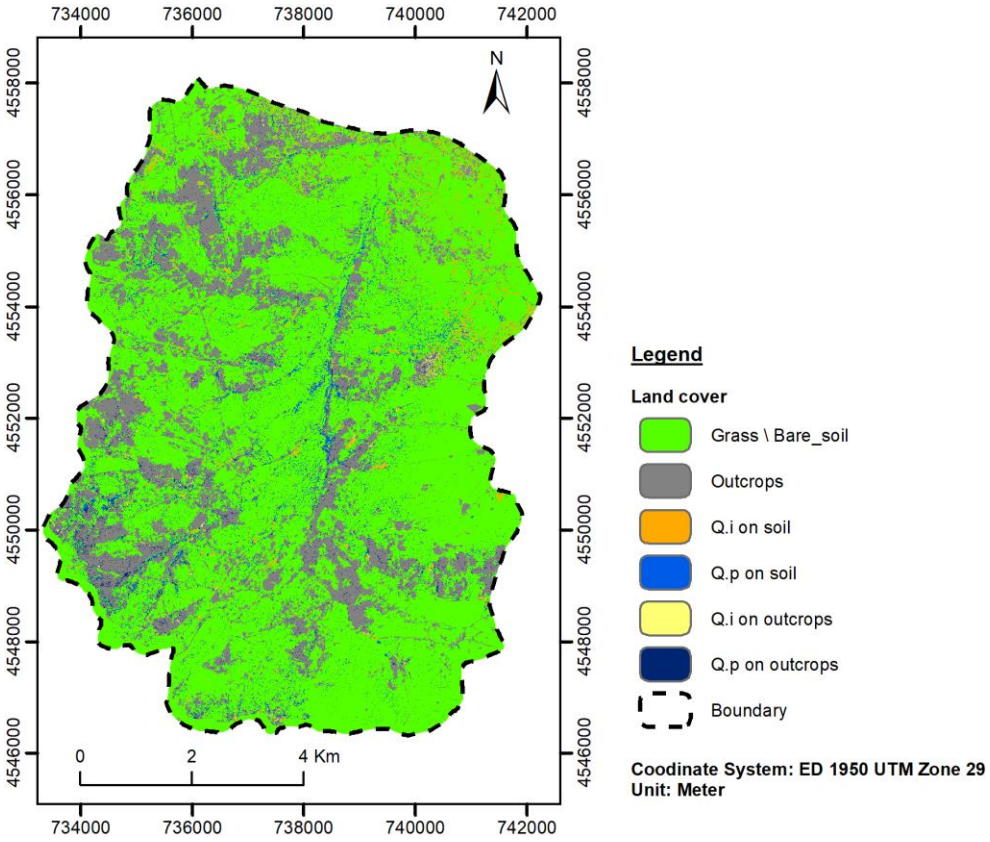

Figure 2.3 Land classification map (Daoud, 2020)

2.4. Hydrology and hydrogeology

The Sardon catchment is characterised by a dense fault network, which plays an important role in the drainage process. Francés et al. (2014) identified the fault network by applying a high pass filter on a high spatial resolution digital terrain model (DTM), as shown in Figure 2.4. Streams follow the secondary faults and flow towards the central Sardon river, which is along the main Sardon fault. The main fault divides the catchment into two geomorphologically different parts: a gentler uplifting western part and a steeper, downthrown eastern part. At the western side of the main fault, there is a brittle fracture zone, few tens to more than thousand meters' wide and a few tens of meters deep. This fracture zone is eroded and in-filled with alluvial deposits and weathered materials, which results in a channel-fill structure (Figure 2.5). This channel-fill structure drains groundwater all year round while the surface Sardon river is intermittent (Hassan et al., 2014).

Two permeable layers were identified by Lubczynski and Gurwin (2005), as shown in Figure 2.5. The top unconsolidated layer (also known as the saprolite layer) is comprised of mainly weathered bedrock and thin alluvial or eluvium deposits, and it has limited spatial extent due its wedging near granite outcrops. The second layer (also known as the fissured layer) are permeable fractured granite, which can outcrop the surface in some areas.

Later, Francés et al. (2014) presented a new conceptual model (Figure 2.6), which is applied in this study. The main difference is that six internally uniform zones (compartments) were defined. For each zone, they determined the geometry and aquifer parameters, for example, layer thickness, hydraulic conductivity and storage terms. The thickness of the saprolite layer varies from zero where outcrops are present through

~1-5 m in the non-faulted zones to 45 m along the main Sardon fault. The fissured layer has thickness ranging from 1 m to 112.5 m in the central part of the catchment. As a typical granitic area, the groundwater table is generally shallow. The groundwater level is lower in the river valleys, around 0~3m below ground surface (b.g.s), while deeper at the watershed divides, around 1~12m b.g.s.

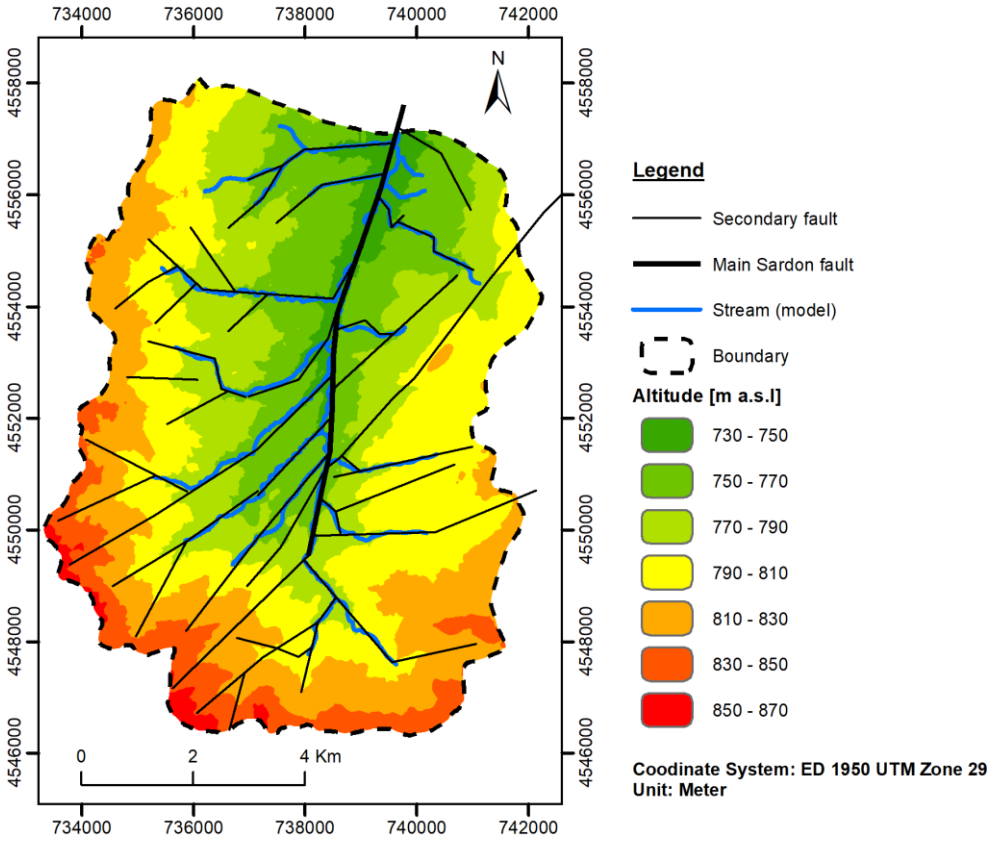

Figure 2.4 The map of fault network (Francés et al., 2014)

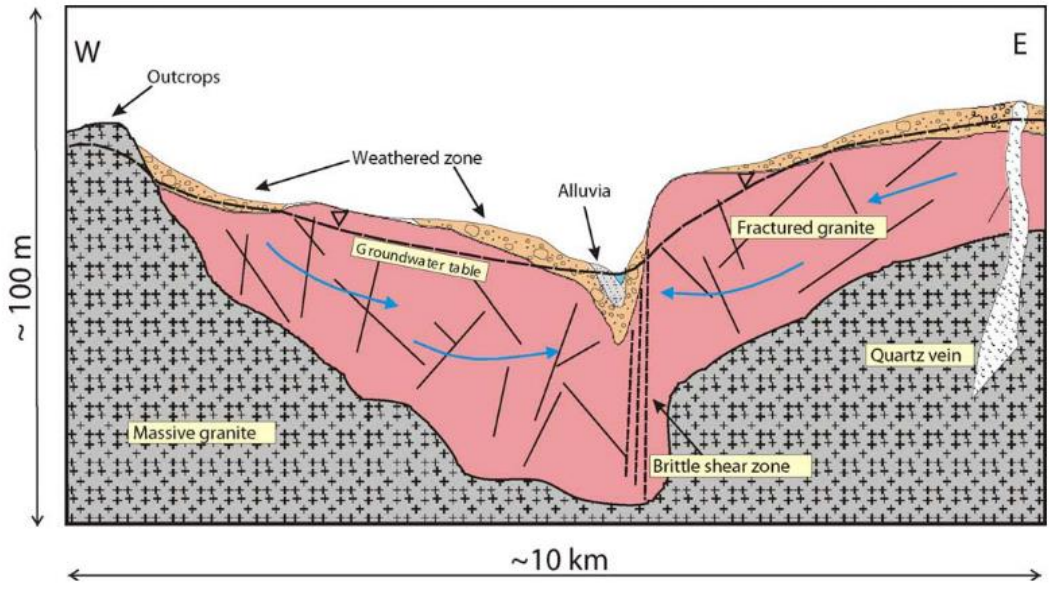

Figure 2.5 Schematic cross-section (Lubczynski and Gurwin, 2005)

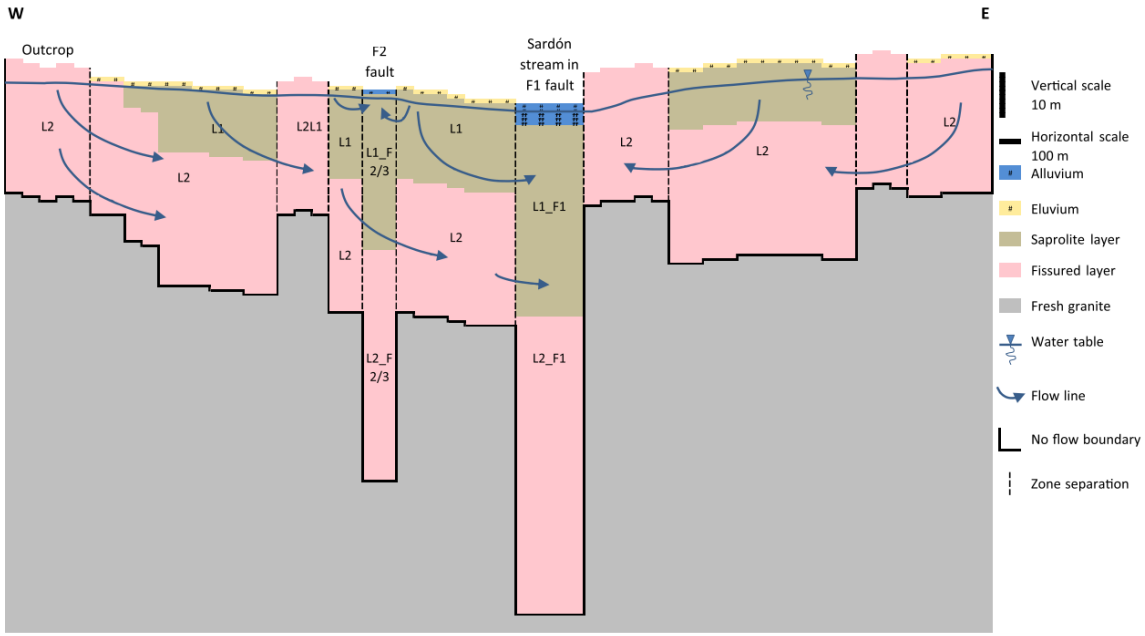

Figure 2.6 Schematic cross-section of the new conceptual model (Francés et al., 2014).

2.5. Monitoring network

In the Sardon catchment, the monitoring network was set up for recording meteorological data, groundwater table and stream discharge, as shown in Figure 2.1.

Two Automated Data Acquisition System (ADAS) stations were installed, i.e. northern ADAS Trabadillo and southern ADAS Meulledes. ADAS is a remotely controlled system comprised of multiple sensors and loggers, providing observed variables in a digital format. In ADAS stations, rainfall is recorded by tipping buckets, and various climatic variables related to evapotranspiration are monitored in an hourly manner, for example, temperature, wind speed, relative humidity, incoming and outgoing radiation. Details about the installation can be found in Lubczynski and Gurwin (2005).

Groundwater table observation sites have been established and gradually increased since 1994. They have various types, for instance, piezometers, wells and boreholes. The groundwater table is hourly recorded continuously, so long-term records are available, which is essential for calibration purposes.

In addition, the stream discharge in the outlet of the catchment was monitored by a steel flume on an hourly basis from 1997 to 2001. The flume was used for measuring low flows due to the relatively low flume capacity of 145 $l.s^{-1}$. Adjacent to the flume, a piezometer was installed for correlating the flow measurement with the piezometric water level. A close linear correlation between the water levels in the piezometer and the water level in a flume was applied for flow calculation (R^2 = 0.9). Therefore, streamflow can be extrapolated during the periods when streamflow was not measured (Hassan et al., 2014).

3. RESEARCH METHOD

3.1. Methodology flowchart

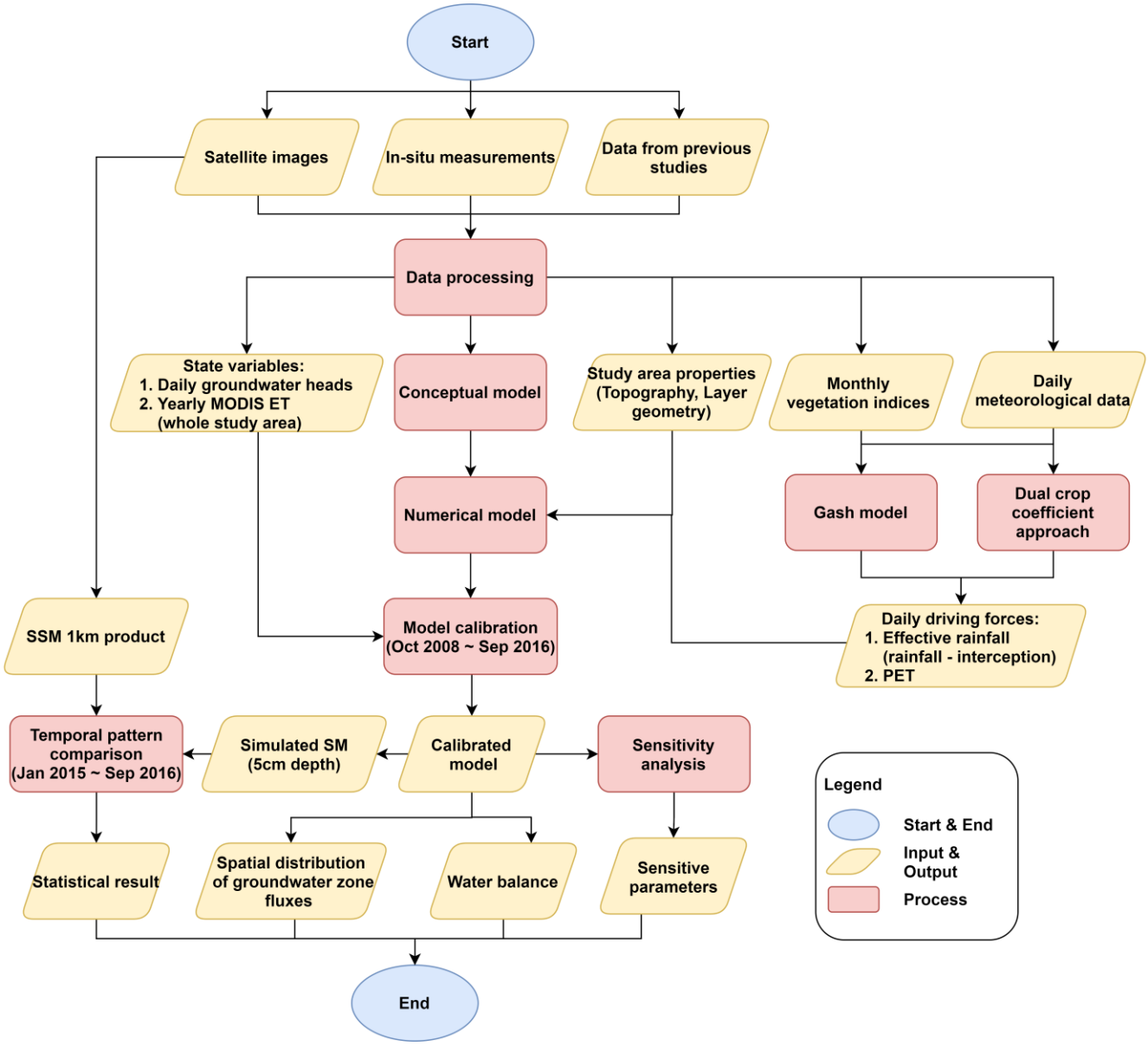

Figure 3.1 Flowchart of methods applied in this study

3.2. Data source

In this study, three types of data were used, i.e., in-situ measurements, satellite images and data from previous studies.

For in-situ measurements, meteorological data from ADAS station was used for calculating driving forces. Groundwater head measurements of 13 distributed sites were retrieved for model calibration. In terms of data from previous studies, for example, layer geometry, DEM and tree interception rate, were used for driving forces calculation and numerical model construction.

Satellite images were retrieved for three purposes：

1. To derive spatio-temporal vegetation indices for driving forces estimation.
2. To calibrate the simulated ET from the model.
3. To compare simulated soil moisture from the model with satellite product.

Table 3.1 Satellite images used in this study

Satellite images	Retrieve period	Source
Landsat 5	2008-10-01 ~ 2010-9-30	EarthExplorer (https://earthexplorer.usgs.gov/)
Landsat 8	2013-10-01 ~ 2015-9-30	EarthExplorer (https://earthexplorer.usgs.gov/)
MODIS16 8-day ET	2008-10-01 ~ 2016-9-30	AppEEARS (https://lpdaacsvc.cr.usgs.gov/appeears/).
SSM1km	2015-01-01 ~ 2016-9-30	Copernicus Global Land Service. (https://land.copernicus.eu/global/products/ssm)

3.3. Conceptual model

3.3.1. Boundaries

The catchment boundaries are characterised as groundwater divides except for the around 1.3 km wide section of the channel-fill outlet (Figure 2.5) at the northern boundary, and this outlet section acts as lateral groundwater outflow (Lubczynski and Gurwin, 2005).

3.3.2. Hydrogeological properties

Francés et al. (2014) identified two permeable layers consistent with the general conceptual model of hard rock aquifers: the top saprolite layer and the underlying fissured layer. Below the fissured layer, they assumed that it is non-fractured bedrock, which represents the impervious bottom boundary. As the heterogeneities of Sardon catchment are controlled by fault zones and weathering process, they defined six internally uniformed zones with aquifer geometry and hydraulic parameters according to the presence of main F1 and F2/F3 fault zones, as shown in Figure 2.6. The layer thickness definition from Francés et al (2014) was followed in this study.

3.3.3. Sources and sinks

For the Sardon catchment, precipitation is the only recharge to the system, while the system outputs are evapotranspiration, stream discharge and lateral groundwater outflow at the outlet of the Sardon river.

3.3.4. Water balance

The hydrological system of this study is characterised as land surface, unsaturated zone and saturated zone. The detailed water balance is as follows:

The equations of water balance of the entire catchment are as follows:

$$P = ET + q + q_g \pm \Delta S \tag{3-1}$$

$$\Delta S = \Delta S_u + \Delta S_g \tag{3-2}$$

where:

P	Precipitation.
ET	Total evapotranspiration.
q	Total streamflow at the catchment outlet.
q_g	Lateral groundwater outflow at the northern boundary of the catchment.
ΔS	Total storage change, which includes unsaturated and saturated zones.
ΔS_u	Unsaturated zone storage change.
ΔS_g	Groundwater zone storage change.

The equations of total evapotranspiration (ET) and total streamflow (q) are as follows:

$$ET = E_{sf} + ET_u + ET_g + RI^e + Exf_{gw}^e \tag{3-3}$$

$$q = RI^s + Exf_{gw}^s + q_B \tag{3-4}$$

$$q_B = q_{gs} - q_{sg} \tag{3-5}$$

where:

E_{sf}	Evaporated canopy interception.
ET_u	Unsaturated zone evapotranspiration.
ET_g	Groundwater evapotranspiration.
RI^e	Rejected infiltration evapotranspired.
Exf_{gw}^e	Groundwater exfiltration evapotranspired.
RI^s	Rejected infiltration routed to streams.
Exf_{gw}^s	Groundwater exfiltration routed to streams.
q_B	Baseflow.
q_{gs}	Groundwater leakage to streams.
q_{sg}	Stream leakage to groundwater.

The equations of land surface and unsaturated zone are as follows:

$$P_e = RI + ET_u + R_g \pm \Delta S_u \tag{3-6}$$

$$P_e = P - E_{sf} \tag{3-7}$$

$$RI = RI^e + RI^s \tag{3-8}$$

where:

P_e	Effective precipitation (infiltration).
RI	Rejected infiltration.
ET_u	Unsaturated zone evapotranspiration.
R_g	Gross groundwater recharge.

The equations of groundwater zone are as follows:

$$R_g + q_{sg} = Exf_{gw} + ET_g + q_{gs} + q_g \pm \Delta S_g \tag{3-9}$$

$$Exf_{gw} = Exf_{gw}^{e} + Exf_{gw}^{s} \tag{3-10}$$

$$R_n = R_g - Exf_{gw} - ET_g \tag{3-11}$$

where:

Exf_{gw} Groundwater exfiltration.

R_n Groundwater net recharge.

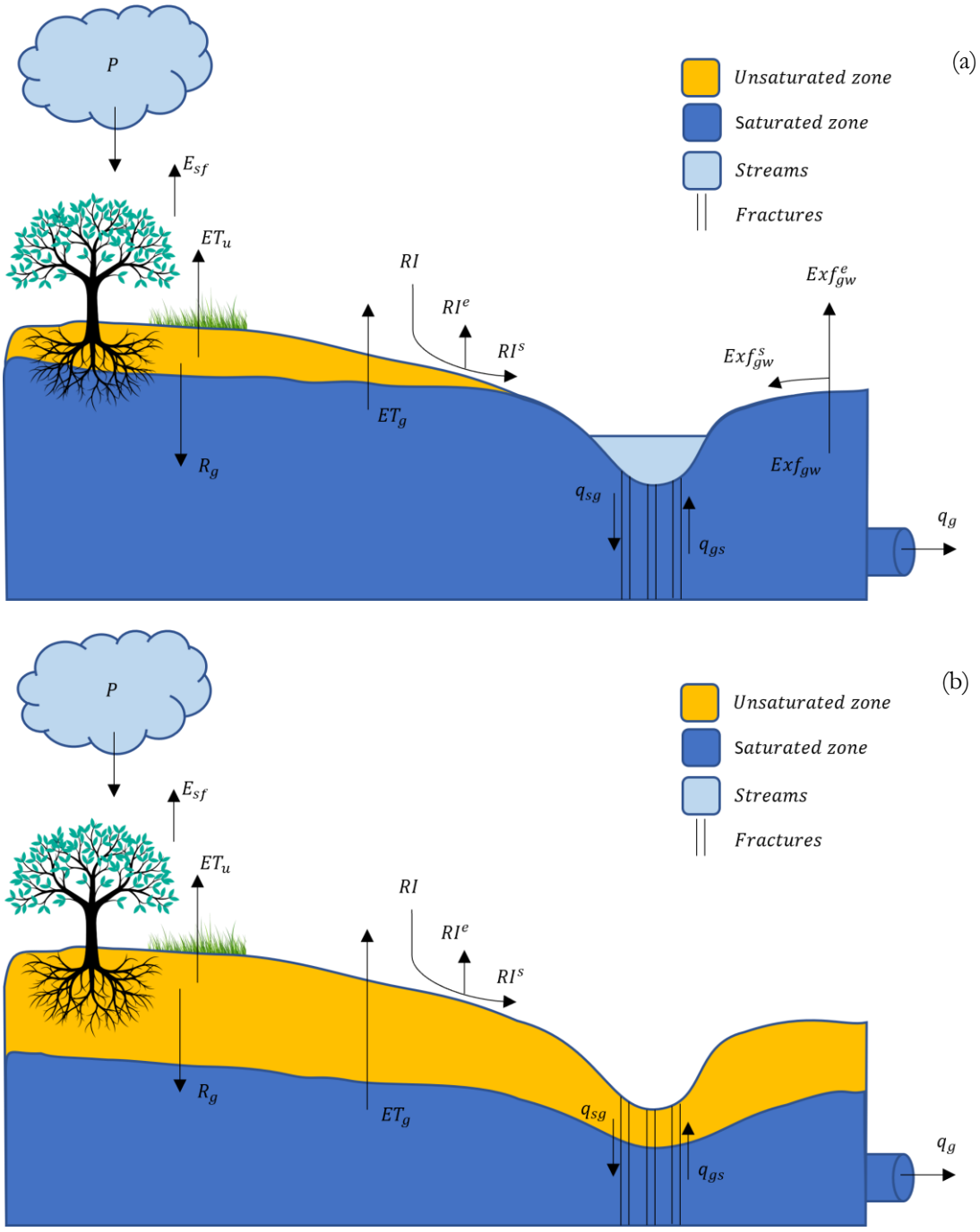

Figure 3.2 Schematic diagram of hydrological components in different seasons: (a) wet seasons; (b) dry seasons (modified from Daoud (2020)).

3.4. Driving forces

For IHM, effective precipitation (also referred to as infiltration) and potential evapotranspiration (PET) are the two important driving forces.

The concept of representative years was introduced for estimation of driving forces applying remote sensing techniques, because vegetation may show similar temporal development in dry years and wet years. In this study, the temporal vegetation development (vegetation indices) captured by remote sensing techniques for representative dry and wet years were assumed to be applicable for other dry and wet years.

As shown in Figure 3.3, an obvious yearly rainfall difference can be observed during the model simulation period. Therefore, simulation years were characterised as dry years and wet years, as shown in Table 3.2.

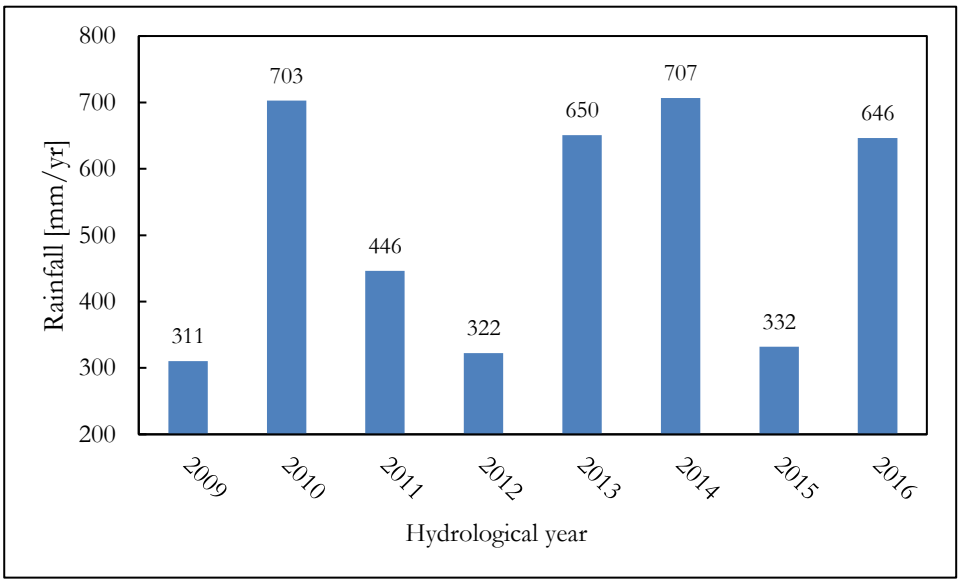

Figure 3.3 Yearly rainfall during the model simulation period (2009 ~ 2016)

Table 3.2 Definition of dry and wet years

Hydrological year	Year type
2009	dry
2010	wet
2011	dry
2012	dry
2013	wet
2014	wet
2015	dry
2016	wet

3.4.1. Effective precipitation (Infiltration)

In this study, effective precipitation is referred to the portion of rainfall reaching the ground after canopy interception. In this case, effective precipitation (precipitation – interception) represents the input to the unsaturated zone in IHM.

As Lubczynski and Gurwin (2005) confirmed that no statistically significant differences were found regarding the spatial distribution of rainfall, the daily rainfall records from the Trabadillo ADAS station were used to represent uniform rainfall in the study area.

As introduced in section 2.3, the main vegetation types are oak trees (*Q.i* and *Q.p*) and grass in the study area. Therefore, it is important to determine interception rates for both trees and grass. Time series of tree interception rates were retrieved from Hassan et al. (2017).

For grass interception, Daoud (2020) applied the revised Gash analytical model, and time-series of Sentinel-2 images were used to retrieve leaf area index (LAI) in order to reflect temporal vegetation characteristics. However, he only calculated canopy storage capacity from LAI for one year and assumed the fractional vegetation cover (c) as 0.5 for implementing the revised Gash analytical model. In this study, the same approach of the Gash revised model was followed for grass interception estimation, but long-term canopy storage capacity and fractional vegetation cover were retrieved.

The Gash model considers rainfall to occur as a series of discrete events and each event comprises three periods: i) wetting up period when the rainfall is less than the threshold value of rainfall required to saturate the canopy; ii) saturation period when rainfall rate > 0.5 mm hr^{-1} (Gash, 1979); iii) drying out period after rainfall ceases. As it would be time-consuming to partition three periods for each rainfall event, total daily rainfall was used for model calculation, assuming one storm per rainy day. Gash et al. (1995) also mentioned this assumption for practical implementation. The formulas of Gash model are shown below.

Gash model:

$$P_G^{'} = -\frac{\bar{R}S_c}{\bar{E}_c}\ln\left[1-\frac{\bar{E}_c}{\bar{R}}\right] \tag{3-12}$$

$$S_c = S/c \tag{3-13}$$

$$\bar{E}_c = \bar{E}/c \tag{3-14}$$

$$E_{sf} = \begin{cases} c\sum_{j=1}^{m} P & \text{for m small storms, } P < P_G^{'} \quad (3\text{-}15) \\ (ncP_G^{'} - ncS_c) + (c\bar{E}_c/\bar{R})\sum_{j=1}^{n}(P - P_G^{'}) + ncS_c & \text{for n storms, } P \geq P_G^{'} \quad (3\text{-}16) \end{cases}$$

where:

$P_G^{'}$	Amount of rainfall required to saturate the canopy	[mm d^{-1}]
P	Total daily precipitation	[mm d^{-1}]
E_{sf}	Canopy interception	[mm d^{-1}]
$\bar{R}$	Mean rainfall intensity =P/24	[mm hr^{-1}]
E	Daily evaporation (calculated by Penman-Monteith method)	[mm d^{-1}]
$\bar{E}$	Mean evaporation rate = E/24	[mm hr^{-1}]

$\bar{E}_c$	Mean evaporation rate per unit area of canopy	[mm hr^{-1}]
c	Fractional vegetation cover	[-]
S	Canopy storage capacity	[mm]
S_c	Canopy storage capacity per unit area of canopy	[mm]

The validity of LAI & S relation has been proven to be effective by previous studies (Keim et al., 2006; Vegas Galdos et al., 2012). Menzel (1997) proposed a LAI & S empirical equation of grassland, and the validity of this equation was proven by Vegas Galdos et al. (2012). Even though this empirical equation cannot be verified in our study area due to lack of field data, it is assumed that this equation is applicable in this study.

Menzel's formula: $$S = 1.2 \cdot \log(1 + LAI) \quad (3\text{-}17)$$

where:

S	Canopy storage capacity	[mm]
LAI	Leaf area index	[-]

In order to retrieve grass LAI and fractional vegetation cover (c), the Biophysical Processor toolbox from SNAP software was used. Biophysical Processor is based on a trained artificial neural network (ANN), and it does prediction based on spectral information. Details about the Biophysical Processor can be found in http://step.esa.int/docs/extra/ATBD_S2ToolBox_V2.0.pdf.

Biophysical Processor supports both Sentinel-2 and Landsat 8 images. However, as Sentinel-2 images are only available from June 2015, Landsat 8 images were selected in order to cover one dry year and one wet year. Time-series of Landsat 8 Collection 1 level 2 images (total 25 cloud-free images) were downloaded for the dry year 2015 and the wet year 2016. Because Landsat 8 images are newly supported by Biophysical Processor and cannot be directly used as inputs for Biophysical Processor, some preprocessing procedures were taken, which are not mentioned in the Help document of Biophysical Processor.

Preprocessing steps:

1. Download viewing angle information from Landsat 8 Collection 2 Level 1 products. Note that the digital value of view angle images is scaled by 100.
2. Add view angle images as new bands to corresponding Landsat 8 images by applying Band Math tool in SNAP software. Because the Biophysical Processor has specific requirements for the name of view angle bands, the new band names were specified as view_zenith_mean, view_azimuth_mean, sum_zenith and sun_azimuth.

In order to consider the spatial representative LAI and c for grass, the representative pixel concept was followed. By combining the land cover map (Figure 2.1) and generated LAI maps, the grass percentage of each pixel of LAI maps can be calculated. Pixels fully covered by grass were referred to as representative grass pixels. Then, the LAI values from grass pixels (around 14000 pixels per image) were averaged to produce representative grass LAI for the whole study area. The same idea was followed by generating representative c values for grass. Because of limited cloud-free images, monthly LAI and c values for two years were derived, and it was assumed that these values of the dry year 2014 and of the wet year 2015 are representative for other dry years and wet years, respectively.

With monthly LAI, monthly S was calculated by applying Eq. (3-17). For simplicity, it was assumed that S and c remain constant for each month. Then, the daily grass interception rate was calculated by applying the Gash model.

3.4.2. Potential evapotranspiration

In IHM, potential evapotranspiration (PET) is an important input for the UZF package to calculate actual evapotranspiration that occurred from unsaturated and saturated zones. Therefore, it is important to implement spatio-temporal variable PET in the model.

In order to consider different vegetation types in the study area, it was assumed that ET_c represents PET in this study. For calculating ET_c, the dual crop coefficient approach from FAO 56 guidelines (Allen et al., 1998) was followed.

FAO Penman-Monteith equation:

$$ET_o = \frac{0.408\Delta(R_n - G) + \gamma \frac{900}{T + 273} u_2 (e_s - e_a)}{\Delta + \gamma(1 + 0.34u_2)} \quad (3\text{-}18)$$

where:

ET_o	Reference evapotranspiration	[mm d^{-1}]
R_n	Net radiation at the crop surface	[MJ m^{-2} d^{-1}]
G	Soil heat flux density	[MJ m^{-2} d^{-1}]
T	Mean daily air temperature at 2 m height	[° C]
u_2	Wind speed at 2 m height	[m s^{-1}]
e_s	Saturation vapour pressure	[kPa]
e_a	Actual vapour pressure	[kPa]
$e_s - e_a$	Saturation vapour pressure deficit	[kPa]
Δ	Slope vapour pressure curve	[kPa ° C^{-1}]
γ	Psychrometric constant	[kPa ° C^{-1}]

For calculating daily ET_o, the required meteorological data was retrieved from the ADAS station.

Dual crop coefficient approach:

$$ET_c = K_c \cdot ET_o \quad (3\text{-}19)$$

$$K_c = K_{cb} + K_e \quad (3\text{-}20)$$

where:

ET_c	Crop evapotranspiration	[mm d^{-1}]
ET_o	Reference evapotranspiration	[mm d^{-1}]
K_c	Crop coefficient	[-]
K_{cb}	Basal crop coefficient	[-]
K_e	Soil evaporation coefficient	[-]

Basal crop coefficient (K_{cb}) is related to vegetation types. Because the FAO 56 does not provide K_{cb} values for natural vegetation as in our study area, the investigation was made to retrieved representative K_{cb} values for each land cover type.

A review by Glenn et al. (2011) indicates the validity of retrieving K_{cb} by vegetation indices (VI). Some researchers have studied the $K_{cb}-VI$ relation of natural vegetation in the Mediterranean dehesa landscape as Sardon catchment (Campos et al., 2013; Carpintero et al., 2020). Even though these empirical $K_{cb}-VI$ equations cannot be verified in the Sardon catchment due to lack of field data, it was assumed that these equations were applicable in this study because of similar climate and landscape.

For grass (Campos et al., 2013):

$$K_{cb} = (1.44 \cdot NDVI) - 0.1 \tag{3-21}$$

where:

K_{cb}	Basal crop coefficient	[-]
$NDVI$	Normalised difference vegetation index	[-]

For oak trees (Carpintero et al., 2020):

$$K_{cb} = \frac{K_{cb-full}}{f_{ceff-full}} \left(\frac{SAVI - SAVI_{\min}}{SAVI_{\max} - SAVI_{\min}} \right), \; if \quad f_c < f_{ceff-full} \tag{3-22}$$

$$K_{cb} = K_{cb-full}, \; if \quad f_c \geq f_{ceff-full} \tag{3-23}$$

$$f_c = \frac{SAVI - SAVI_{\min}}{SAVI_{\max} - SAVI_{\min}} \tag{3-24}$$

where:

K_{cb}	Basal crop coefficient	[-]
$f_{ceff-ful}$	Ground cover fraction when K_{cb} reaches its maximum ($K_{cb-full}$). 0.8 was used in this study.	[-]
$K_{cb-full}$	The maximum K_{cb}. 1.6 was used in this study.	[-]
$SAVI$	Soil adjusted vegetation index	[-]
$SAVI_{\max}$	$SAVI$ for high LAI. 0.59 was used in this study.	[-]
$SAVI_{\min}$	$SAVI$ for bare soil. 0.09 was used in this study.	[-]

In order to derive $SAVI$ and $NDVI$, time-series of Landsat 5 images (total 21 cloud-free images) were downloaded for the dry year 2009 and the wet year 2010. Representative $SAVI$ and $NDVI$ values for different land cover types were derived by the method of searching representative pixels as mentioned in Section 3.4.4.1. The calculated monthly $SAVI$ and $NDVI$ values for 2009 and 2010 were assumed to be applicable for other dry years and wet years, respectively. Then, monthly K_{cb} for different land cover types were generated.

Soil evaporation coefficient (K_e) estimation are based on the previous study. Time-series of subsurface evaporation (E_{ss}) simulated by HYDRUS1D model was retrieved for the dry year 2009 and the wet year 2010 (Balugani et al., 2017). As Balugani et al. (2017) calculated actual soil evaporation, the time series of E_{ss} was multiplied by an assumed factor of 1.5 to represent the potential soil evaporation. Then, by diving E_{ss} by ET_o, monthly K_e was calculated for grass/bare soil land cover.

Moreno et al. (2005) studied the oak tree root distribution in the dehesa of Spain, and they noticed that the lateral extent of *Q.ilex* tree roots can be even 7 times the projection of the canopy. The large root extent may indicate the dominant role of oak trees in water extraction in a typical dry environment. Therefore, in this study, it is assumed that K_e is zero for the canopy projection of both *Q.ilex* and *Q.pyrenica*, either on soil or on outcrops. The equations for calculating K_c for each land cover type are shown in Table 3.3.

Table 3.3 K_c calculation for different land cover types

Land cover type	Calculation of K_c
Grass/ bare soil	$K_c = K_e + K_{cb}$
Outcrops	$K_c = 0.5 \cdot K_e \ (K_{cb} = 0)$
Q.ilex on soil	$K_c = K_{cb} \ (K_e = 0)$
Q.ilex on outcrops	$K_c = K_{cb} \ (K_e = 0)$
Q.pyrenica on soil	$K_c = K_{cb} \ (K_e = 0)$
Q.pyrenica on outcrops	$K_c = K_{cb} \ (K_e = 0)$

3.5. Numerical model

3.5.1. Code and software selection

In this study, MODFLOW 6, the latest MODFLOW code, was applied. MODFLOW 6 is based on a control-volume finite-difference (CVFD) method, and it supports both standard formulation and Newton-Raphson formulation. As Newton-Raphson formulation has the advantage in solving cell drying and wetting nonlinearities of the unconfined groundwater equations, Newton-Raphson formulation was activated in this study. Details about MODFLOW 6 formulation can be found in Langevin et al. (2017).

For model input preparation and output post-processing, MODFLOW 6 is supported by two official open-source software, i.e., ModelMuse and Flopy. ModelMuse is a graphical user interface (GUI), which provides ease for users to construct and visualise the model. Details can be found in the documentation of ModelMuse (Winston, 2019). Flopy is a Python code developed by Bakker et al. (2016). Flopy has the advantage of directly manipulating model input files and facilitating analyses that can be difficult for GUIs. In this study, ModelMuse was selected for building the numerical model.

3.5.2. Grid setup

Except for the standard rectangular grid, MODFLOW 6 also supports the unstructured grid approach, which means that a model cell can be hydraulically connected to an arbitrary number of adjacent cells. The unstructured grid approach benefits local refinement of the area of interest, for example, rivers, streams and wells, but also observation points. Various grid types are supported by MODFLOW 6, for instance, Voronoi grid, Quadtree grid and nested grid. These grids with spatially varying geometry can better represent the area of interest with irregular boundaries compared with the standard rectangular grid. In this study, the unstructured Quadtree grid approach was used.

For grid setup, first, a structured grid with 100×100 m cell size for two layers was created. As ModelMuse only supports Quadtree grid up to now, then local Quadtree refinement was applied to streams and groundwater head monitoring sites. At the end, for each layer, the total cell number was 19561, and cell size ranges from 25 × 25 m to 100 × 100 m.

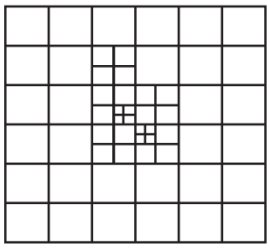

Figure 3.4 An example of Quadtree grid

For vertical discretisation, model top elevation and layer thickness are required. Layer thickness raster maps were retrieved from Francés et al. (2014). As the layer thickness map does not indicate the location of outcrops with zero thickness in the first layer, further processing was taken. First, by combining the outcrop map from Francés et al. (2014) and the model grid, the statistics of outcrop percentage for each model cell was calculated. Then, the issue was to define the threshold of outcrop percentage for identifying cells representing outcrops. The threshold was determined by several manual trials, matching the total area of the outcrop cells in the model with the total outcrop area in the outcrop map. After identifying outcrop cells, the layer thickness was set to zero in the first layer for those cells. In order to exclude these outcrop cells of the first layer from simulation, the IDOMAIN value was set to -1 for making outcrop cells as vertical pass-through cells in the first layer. All model cells in the second layer remained as active cells (IDOMAIN = 1). Details about IDOMAIN can be found in the spatial discretisation chapter in Langevin et al. (2017)

For model elevation, the top elevation of the first layer was assigned by a 5 m resolution digital elevation model (DEM) retrieved from the Spanish Centro Nacional de Informacíon Geográfica (www.cnig.es). As the DEM has a higher spatial resolution than the model grid, averaged values inside each model cell were applied. Then, the elevation of each layer was calculated by subtracting layer thickness as equations shown below.

$$Bot_1 = Top_1 - D_1 \tag{3-25}$$

$$Bot_2 = Top_2 - D_2 \tag{3-26}$$

$$Top_2 = Bot_1 \tag{3-27}$$

where:

Top_1	Top elevation of the first layer.	[m]
Top_2	Top elevation of the second layer.	[m]
Bot_1	Bottom elevation of the first layer.	[m]
Bot_2	Bottom elevation of the second layer.	[m]
D_1	Thickness of the first layer	[m]
D_2	Thickness of the second layer	[m]

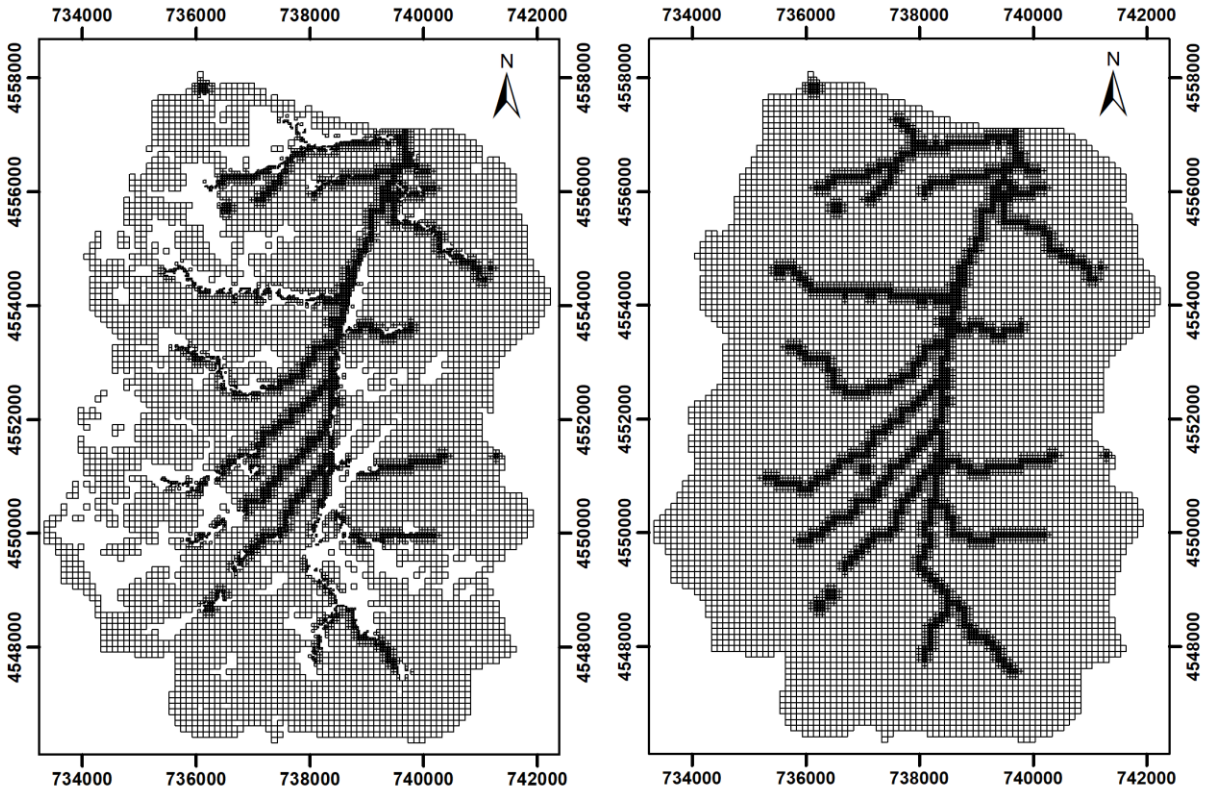

Figure 3.5 Model grid setup: (a) active cells of the first layer; (b) active cells of the second layer.

3.5.3. Time discretisation

In this study, a transient model covering 8 hydrological years (1 October 2008 to 30 September 2016) was created. Daily time step and daily stress period were applied, in total 2922 actual stress periods. Prior to the actual study period, the first hydrological year with 365 stress periods were duplicated as a spin-up period and added to the simulation process. Consequently, the total simulation period became 9 years (1 spin-up year + 8 actual years) with 3287 stress periods.

3.5.4. Hydraulic properties

In MODFLOW 6, Node Property Flow (NPF) package calculates internal flow and defines hydraulic conductivity, including horizontal hydraulic conductivity (K_h) and vertical hydraulic conductivity (K_v). In this study, the harmonic mean method was selected for transmissivity calculation, and isotropic horizontal hydraulic conductivity was assumed ($K_h = K_x = K_y$). The K_h for both layers were assumed as 0.05 m d^{-1} as an initial value, and K_v for both layers were assumed as 0.01 m d^{-1} as an initial value. Both K_h and K_v were adjusted during the calibration by a group of zones for each layer.

The storage package (STO) package simulates the contribution of confined and unconfined storage changes to the groundwater head change. The parameters required by the STO package are specific yield (S_y) and specific storage (S_s). For both layers, the initial values for S_y and S_s were assumed as 0.05 and 10^{-5} m^{-1}, respectively. Both S_y and S_s were adjusted during the calibration by a group of zones for each layer.

As the unstructured grid approach was applied, the Ghost Node (GNC) package was activated in order to correct internal flow and head calculation. Details about the GNC package can be found in Langevin et al. (2017).

3.5.5. Boundary conditions

3.5.5.1. Unsaturated zone (UZF) package

The UZF package simulates vertical flow through the unsaturated zone and adds the resulting recharge to the saturated zone. The UZF package is based on the kinematic wave approximation of Richards' equation, and negative pressure gradients are ignored for simplicity (Langevin et al., 2017).

The simplified equation is expressed as below:

$$\frac{\delta\theta}{\delta t} + \frac{\delta K(\theta)}{\delta z} + i_{ET} = 0 \tag{3-28}$$

where:

θ	Volumetric water content	[$L^3 L^{-3}$]
t	Time	[T]
$K(\theta)$	Vertical unsaturated hydraulic conductivity as a function of water content	[$L T^{-1}$]
i_{ET}	The unsaturated zone ET rate per unit depth	[$LT^{-1}L^{-1}$]

Two main inputs for the UZF package are land surface driving forces, i.e., infiltration rate and PET, which are calculated in Section 3.4. In the UZF package, the specified infiltration rate is converted to water content as shown in Eq.(3-30), but the water input into subsurface is constrained by vertical saturated hydraulic conductivity (K_{sat}). If the specified infiltration rate is equal to or exceeds K_{sat}, the water content of the uppermost trailing wave is set to θ_{sat}. Besides, if the specified infiltration rate is greater than K_{sat}, then the difference between the specified infiltration rate and K_{sat}, so called rejected infiltration (RI) is multiplied by the corresponding model cell area and this volumetric rate of water can be added to other features, for example, streams, lake and well, by MVR package. In such case, RI can be simulated as overland flow. However, part of RI can also be evapotranspired.

$$K(\theta) = K_{sat}\left[\frac{\theta - \theta_{resid}}{\theta_{sat} - \theta_{resid}}\right]^{\varepsilon} \tag{3-29}$$

$$\theta_{qa} = \left(\frac{q_a}{K_{sat}}\right)^{1/\varepsilon}\left(\theta_{sat} - \theta_{resid}\right) + \theta_{resid} \qquad 0 < q_a \le K_{sat} \tag{3-30}$$

$$\theta_{qa} = \theta_{sat} \qquad q_a > K_{sat}$$

where:

K_{sat}	Saturated hydraulic conductivity	[$L T^{-1}$]
θ_{resid}	Residual (irreducible) water content	[$L^3 L^{-3}$]
θ_{sat}	Saturated water content	[$L^3 L^{-3}$]
ε	Brooks-Corey exponent	[-]
θ_{qa}	Corresponding water content to specified infiltration rate	[$L^3 L^{-3}$]
q_a	Specified infiltration rate	[$L T^{-1}$]

For evapotranspiration simulation, the UZF package first satisfies PET by removing water from the unsaturated zone, but no more water would be removed from the unsaturated zone if the water content in the unsaturated zone reduces to θ_{resid}. If PET is not yet satisfied by unsaturated zone water content and also water table is above the specified extinction depth (d_{ext}), the remaining PET demand is subtracted from the saturated zone. In that case, both unsaturated zone evapotranspiration (ET_u) and groundwater evapotranspiration (ET_g) are simulated.
The UZF package supports also simulation of groundwater exfiltration (Exf_{gw}) by defining surface depth (d_{surf}), which is a user-specified depth relative to the land surface where groundwater exfiltration starts. More details about the UZF package can be found in Langevin et al. (2017).

In this study, spatio-temporally variable infiltration rate and PET were applied by a weighted average approach. As in Section 3.4, PET and interception rate for different land cover types were calculated, following the weighted influence of each land cover inside each model cell. Therefore, for each model cell, the formula for calculating PET and infiltration is shown as follows.

$$PET = \sum_{i=1}^{6} PET_i \cdot c_i \tag{3-31}$$

$$q_a = P - \sum_{i=1}^{6} E_{sf\,i} \cdot c_i \tag{3-32}$$

where:

PET_i	PET rate for six land cover types	[mm d^{-1}]
c_i	Percentage of each model cell that is covered by six land cover types.	[m^2 m^{-2}]
E_{sf-i}	Interception rate for six land cover types. Note that $E_{sf} = 0$ for outcrops.	[mm d^{-1}]
P	Precipitation	[mm d^{-1}]

Regarding extinction depth for each vegetation, it is assumed that *Q.ilex* and *Q.pyrenica* have an extinction depth of 3.7 m, and grass has an extinction depth of 1 m. The extinction depth for outcrops is zero. For implementing extinction depth for each model cell, the same weighted average approach was followed.

$$d_{ext} = \sum_{i=1}^{6} d_{ext-i} \cdot c_i \tag{3-33}$$

where:

d_{ext-i}	Extinction depth for six land cover types	[mm d^{-1}]
c_i	Percentage of each model cell that is covered by six land cover types.	[m^2 m^{-2}]

For the UZF package, the initial values were assumed as Table 3.4 and later were adjusted during model calibration.

Table 3.4 Parameters for UZF package

Parameter		Value	Unit
K_{sat}	Vertical saturated hydraulic conductivity	equal to K_v	[m^3 m^{-3}]
θ_{ini}	Initial water content	0.15	[m^3 m^{-3}]
θ_{sat}	Saturated water content	0.4	[m^3 m^{-3}]
θ_{resid}	Residual water content	0.05	[m^3 m^{-3}]
ε	Brooks-Corey exponent	3.5	[-]
d_{surf}	Surface depth	0.125	[m]

3.5.5.2. Streamflow routing (SFR) package

The SFR package was applied to simulate flow interaction between groundwater and streams. For calculating streamflow, two options are available in the SFR package, i.e., i) active reaches option; ii) simple routing reaches option. Active reaches option calculates flow based on calculated stream depth inside the model, while the simple routing reaches option calculates flow based on user-specified stream depth. In this study, the active reaches option was applied.

For the SFR package, the required inputs are reach length, reach width, reach gradient, streambed top elevation, streambed thickness and streambed hydraulic conductivity and Manning coefficient. For reach length, it is automatically calculated inside ModelMuse. For reach gradient, it was calculated in ArcGIS by combing the stream shapefile and DEM mentioned in Section 3.5.2. Streambed top elevation was assigned as 2 m below the model top for Sardon river and 1m below the model top for tributaries. Streambed thickness was assumed as 0.2 m for all stream reaches. The reach width was assumed 5 m for tributaries and 10 m for the Sardon river. Manning coefficient was assigned as 0.035 for all stream reaches. The streambed hydraulic conductivity (K_b) was assumed to be equal to K_v of the underlying model cell.

3.5.5.3. Drain (DRN) package

In this study, the drain package was activated for simulating later groundwater outflow around the area of the outlet of Sardon river. The drain package acts as a head-dependent boundary, and it removes water from the aquifer based on the drain conductance and the difference between drain elevation and head.

$$Q_{out} = C_d \cdot \left(h_{aq} - h_d \right) \qquad h_{aq} > h_d \tag{3-34}$$

$$Q_{out} = 0 \qquad h_{aq} \le h_d \tag{3-35}$$

$$C_d = K_d A_\perp / b_d \tag{3-36}$$

where:

Q_{out}	Flow from the aquifer to drain	[$m^3 d^{-1}$]
C_d	Drain conductance	[$m^2 d^{-1}$]
K_d	Hydraulic conductivity of drain bed	[$m d^{-1}$]
$A_\perp$	Area perpendicular to the flow = cell width * cell thickness	[m^2]
b_d	Drain bed thickness	[m]
h_{aq}	Head in the drain cells	[m]
h_d	Drain elevation	[m]

Drain elevation and drain bed thickness was assigned as 733 m and 0.5 m, respectively. Hydraulic conductivity of the drain bed was assumed to be equal to K_v of the model cell contains the drain. The initial values for drain bed conductance varied from 12.5 to 200 $m^2 d^{-1}$ due to different cell sizes and were later adjusted during model calibration.

3.5.5.4. Water mover (MVR) package

The MVR package is a new package developed for MODFLOW 6, and it is designed to move water from one package to another. The MVR package is based on the concept of "providers" and "receivers". The providers send available water to the MVR package, and then the MVR package distributes that water to receivers, as requested by the user. No water would be transferred if there is no available water from providers or no package features are defined as receivers.

In this study, the MVR package was activated for simulating overland flow and evapotranspiration resulted from rejected infiltration (RI) and groundwater exfiltration (Exf_{gw}). All UZF cells were assigned as providers, and the closest SFR reaches were assigned as receivers. For calculating receiver flow rate, the FACTOR option was selected.

$$Q_R = \alpha \cdot Q_P \tag{3-37}$$

where:

Q_R	Flow rate to the receiver	[$m^3\ d^{-1}$]
Q_P	Available flow rate from the provider	[$m^3\ d^{-1}$]
α	The MVR factor converts the provider flow rate to the receiver flow rate	[-]

The MVR factor determined the portion of rejected infiltration (RI) and groundwater exfiltration (Exf_{gw}) that were transferred to the streams, i.e., rejected infiltration routed to streams (RI^s) and groundwater exfiltration rounted to streams (Exf_{gw}^s), and the remaining portion of water represents the rejected infiltration evapotranspired (RI^e) and groundwater exfiltration evapotranspired (Exf_{gw}^e), which contribute to the total ET.

MVR factor was assigned as 0.5 as the initial value and then was adjusted during calibration. The MVR factor plays an important role in later ET calibration because it affects RI^e and Exf_{gw}^e.

3.5.6. Model calibration

As a general practice, a steady-state model is built and calibrated in order to generate initial conditions for transient simulation. As steady-state model results are not always useful as initial conditions of the transient model and also because transient models are by far more reliable than steady-state models, only transient model calibration was carried out in this study. For a complete model run (1 spin-up year + 8 simulation years), it would take around 13 hours for a laptop that is equipped with 16 GB memory and an i7-10750H CPU.

For transient model calibration, the trial-and-error approach was applied. The calibration parameters are shown in Table 3.5.

Table 3.5 Calibration parameters

Parameter		dependency	Initial values	Unit	Model package	Described in section
K_h	Horizontal hydraulic conductivity		0.05	[m d^{-1}]	NPF	3.5.4
K_v	Vertical hydraulic conductivity		0.01	[m d^{-1}]	NPF	3.5.4
K_{sat}	Vertical saturated hydraulic conductivity	equal to K_v	0.01	[m d^{-1}]	UZF	3.5.5.1
K_b	Streambed hydraulic conductivity	equal to K_v	0.01	[m d^{-1}]	SFR	3.5.5.2
K_d	Drain bed hydraulic conductivity	equal to K_v	0.01	[m d^{-1}]	DRN	3.5.5.3
C_d	Drain bed conductance		12.5 ~ 200	[$m^2\ d^{-1}$]	DRN	3.5.5.3
S_y	Specific yield		0.05	[-]	STO	3.5.4
S_s	Specific storage		10^{-5}	[m^{-1}]	STO	3.5.4
α	MVR factor		0.5	[-]	UZF	3.5.5.1

3.5.6.1. Initial condition

As only a transient model was built, a spin-up period was needed. The spin-up period is a period prior to the simulation period of interest in order to reduce the influence of potentially erroneous starting heads with a sufficient long period (Anderson et al., 2015). In this study, the daily stresses of the first simulation year (1 October 2008 to 30 September 2009) were duplicated and then assigned as the spin-up period.

As the groundwater table depth varies between 0 ~ 3 m along the river valley and between 1 ~ 12 m at the watershed divides (Francés et al., 2014), the starting heads were assigned as 3 m below the model top elevation due to generally shallow groundwater table.

3.5.6.2. Calibration state variables

For the transient calibration, the calibration targets were daily heads and yearly actual evapotranspiration (ET_a) simulated by the model. Daily groundwater head records of 13 monitoring sites were retrieved for calibration purposes.

For ET_a calibration, as the Sardon catchment is relatively small (~ 80km^2), MODIS16 8-day ET product was selected due to long temporal coverage (from 2001 till now) and high spatial resolution of 500 m, which is a relatively high spatial resolution compared with other global ET products, for example, SSEBop (Senay et al., 2013) with 1 km spatial resolution and GLEAM (Martens et al., 2016) with 25km spatial resolution. For MODIS ET product assessment, Velpuri et al. (2013) evaluated MODIS ET product in the United States and concluded the reliability of MODIS ET for hydrologic application. It was assumed that MODIS ET product was valid as the reference for model calibration in this study.

Time series of MODIS16 8-day ET was retrieved to cover the simulation period (1 October 2008 to 30 September 2016). Two processing steps were taken as follows.

Processing steps:

1. Yearly MODIS ET for the whole study area was generated by aggregating time series of 8-day MODIS ET. Yearly MODIS ET was used as the state variable for calibration.
2. Daily MODIS ET for the whole study area was derived by averaging 8-day time series of MODIS ET. Daily MODIS ET was used later to compare with daily simulated ET.

3.5.6.3. Error assessment

For head calibration, mean absolute error (MAE) and root mean square error (RMSE) were used for evaluation. The heads were considered calibrated when MAE ≤ 0.8 m and RMSE ≤ 1 m. For ETa calibration, the yearly difference of ±20% was considered acceptable.

$$MAE = \frac{1}{n}\sum_{i=1}^{n}\left|h_m - h_s\right|_i \tag{3-38}$$

$$RMSE = \sqrt{\frac{1}{n}\sum_{i=1}^{n}\left(h_m - h_s\right)_i^2} \tag{3-39}$$

$$D_{ET} = \frac{ET_s - ET_{MODIS}}{ET_{MODIS}} \tag{3-40}$$

where:

MAE	Mean absolute error	[m]
$RMSE$	Root mean square error	[m]
D_{ET}	Yearly difference between simulated ET and MODIS ET	[%]
h_m	Measured head	[m]
h_s	Simulated head	[m]
ET_s	Simulated yearly ET over the entire catchment	[mm yr^{-1}]
ET_{MODIS}	Yearly MODIS ET over the entire catchment	[mm yr^{-1}]
n	Number of records	[-]

3.5.6.4. Sensitivity analysis

Sensitivity analysis is to test how the model solution would respond to the change in parameters in order to find sensitive parameters. It is performed by changing one parameter incrementally while fixing other parameters. In this study, sensitivity analysis was performed for horizontal hydraulic conductivity, vertical hydraulic conductivity, specific yield and specific storage.

3.6. Comparison of selected satellite soil moisture product with simulated soil moisture from the model

3.6.1. Simulated soil moisture

The UZF package supports extracting simulated volumetric soil moisture at user-defined depth. Therefore, it provides an opportunity to assess the simulated soil moisture generated by a calibrated model. Considering the spatial representativeness, the simulated soil moisture at 5 cm depth was compared with the selected satellite soil moisture product in this study.

3.6.2. Satellite soil moisture

In this study, considering the area of Sardon catchment (~80 km^2), the SSM1km product from Copernicus Land Surface Service (https://land.copernicus.eu/global/products/ssm) was retrieved for the comparison purpose. SSM1km product is based on Sentinel-1 backscatter data and is only available for Europe from 2015. Time-series of SSM1km was downloaded (1 January 2015 to 30 September 2016).

The soil moisture in the SSM 1km represents the degree of saturation in the topmost 5 cm of the soil, but it can be translated from relative (%) to absolute volumetric units ($m^3\ m^{-3}$), using porosity information ($m^3\ m^{-3}$). Details about the SSM1km can be found in the user manual and Bauer-Marschallinger et al (2019). According to the field experiment in Trabadillo ADAS station by Balugani (2021), the soil porosity was taken as 0.4 $m^3\ m^{-3}$ in this study.

Conversion formula:

$$SSM(t) = 0.5 \cdot DN \tag{3-41}$$

$$SSM_a(t) = p\frac{SSM(t)}{100} \tag{3-42}$$

where:

DN	Digital values stored in the raw SSM 1km images	[-]
$SSM(t)$	Relative saturation degree of surface soil moisture for a day	[%]
$SSM_a(t)$	Absolute volumetric surface soil moisture for a day.	[$m^3\ m^{-3}$]
p	Soil porosity	[$m^3\ m^{-3}$]

3.6.3. Daily comparison and statistical metrics

The comparison between simulated soil moisture and satellite soil moisture was performed on one pixel covering the Trabadillo ADAS station. As the model grid has finer spatial resolution than satellite soil moisture, the simulated soil moisture was spatially aggregated to the same spatial resolution as the satellite soil moisture. The comparison was carried out on a daily scale.

Root mean square error ($RMSE$) and Pearson correlation coefficient (r) were used for comparison.

$$RMSE = \sqrt{\frac{1}{n}\sum_{i=1}^{n}\left(x_i - y_i\right)_i^2} \tag{3-43}$$

$$r = \frac{\sum_{i=1}^{n}\left(x_i - \overline{x}\right)\left(y_i - \overline{y}\right)}{\sqrt{\sum_{i=1}^{n}\left(x_i - \overline{x}\right)^2\left(y_i - \overline{y}\right)^2}} \tag{3-44}$$

where:

$RMSE$	Root mean square error	[m^3 m^{-3}]
r	Pearson correlation coefficient	[-]
x_i	Soil moisture from SSM 1km	[m^3 m^{-3}]
$\overline{x}$	Mean value of soil moisture from SSM 1km	[m^3 m^{-3}]
y_i	Simulated soil moisture from the model	[m^3 m^{-3}]
$\overline{y}$	Mean value of simulated soil moisture from the model	[m^3 m^{-3}]
n	Number of comparison dates	[-]

4. RESULTS AND DISCUSSION

4.1. Driving forces

4.1.1. Interception

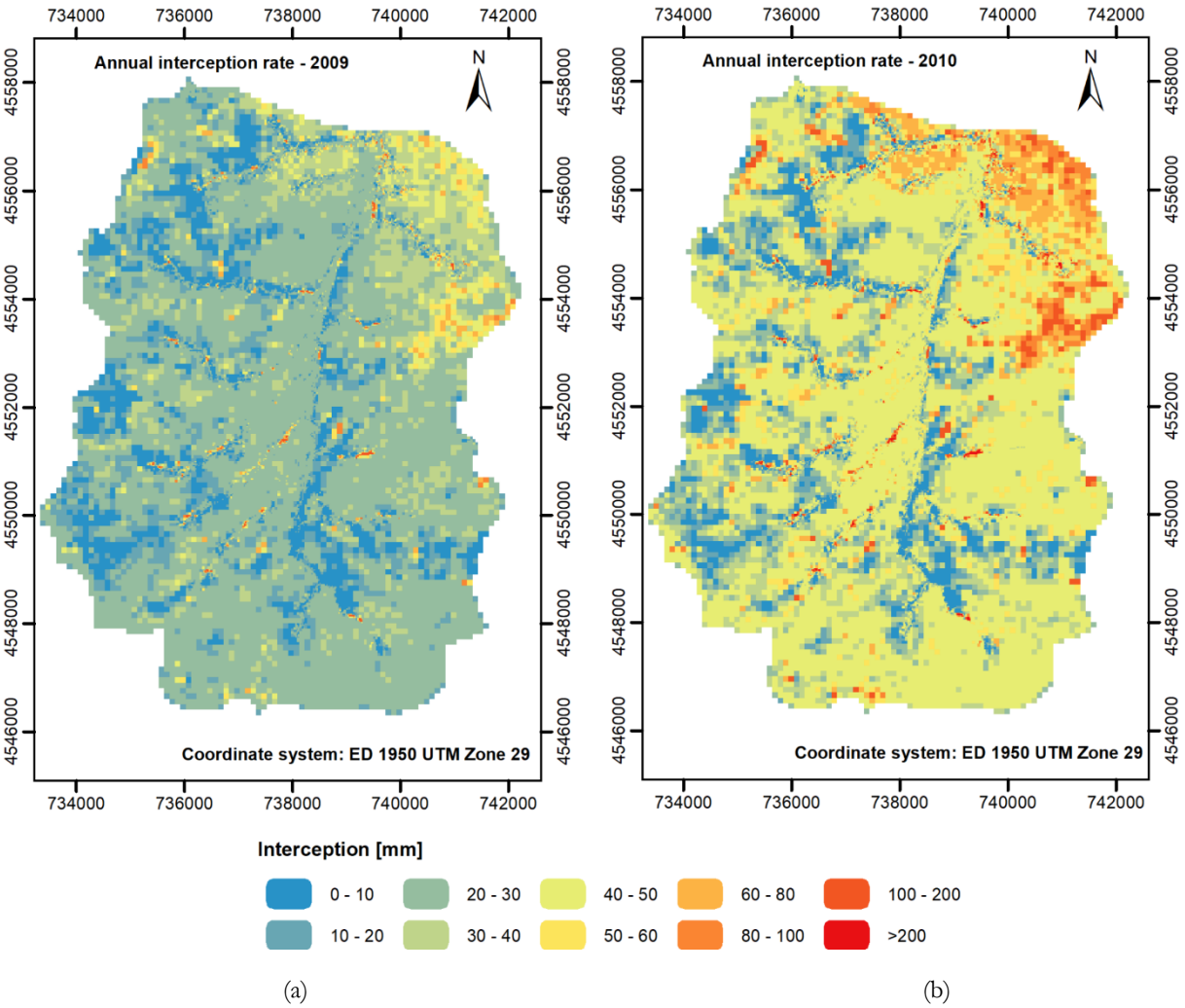

Figure 4.1 Spatial distribution of annual interception rate for the dry year 2009 and the wet year 2010.

As uniform rainfall was used, interception was the key to affecting the spatial distribution of effective rainfall. Figure 4.1 shows the annual interception rate for the dry year 2009 and the wet year 2010. It can be observed that the spatial distribution patterns were similar for both years. The highest interception can be observed in the northeastern part of the study area characterized by dense occurrence of evergreen *Q.i.*, while the lowest in the western and southern parts dominated by grasslands and outcrops, the latter having zero interception. Besides, some sparsely distributed high interception pixels are observed, which are attributed to the groups of either *Q.i.* or *Q.p.* trees.

Large differences in annual interception rate are observed. These differences are mainly attributed to annual differences in rainfall. For example, in the wet year 2010, the annual interception rate in most areas was around 50 ~ 60 mm, while in the dry year 2009, around 20 ~ 30 mm. Moreover, in the wet year 2010,

the highest annual interception rate was above 200 mm in the north-eastern part, in contrast to ~100 mm for the dry year 2009.

Table 4.1 Yearly interception ratio of each land cover type per unit area.

	Estimation based on section 3.4.1	Retrieved from Hassan et al. (2017)				
Year	Grass/ bare soil	Outcrops	*Q.i* on soil	*Q.p* on soil	*Q.i* on outcrops	*Q.p* on outcrops
2009	9.48%	0.00%	59.24%	9.33%	59.24%	9.33%
2010	6.55%	0.00%	52.78%	7.89%	52.78%	7.89%
2011	6.96%	0.00%	54.15%	6.49%	54.15%	6.49%
2012	8.47%	0.00%	51.97%	15.68%	51.97%	15.68%
2013	7.55%	0.00%	46.00%	9.53%	46.00%	9.53%
2014	6.73%	0.00%	53.50%	9.44%	53.50%	9.44%
2015	8.61%	0.00%	55.48%	15.71%	55.48%	15.71%
2016	7.35%	0.00%	49.15%	6.33%	49.15%	6.33%

Table 4.2 Percentage coverage of each land cover type over the entire catchment

Land cover type	Grass/ bare soil	Outcrops	Q.ilex on soil	Q.pyrenica on soil	Q.ilex on outcrops	Q.pyrenica on outcrops
Percentage coverage over the entire catchment	71.58%	21.50%	1.57%	3.51%	0.34%	1.29%

Table 4.3 Yearly interception ratio of each land cover type over the entire catchment

Year	Precipitation [mm]	Total interception [mm]	Grass/ bare soil	Outcrops	*Q.i* on soil	*Q.p* on soil	*Q.i* on outcrops	*Q.p* on outcrops
2009	310.53	25.81	6.79%	0.00%	0.93%	0.33%	0.20%	0.12%
2010	702.69	42.39	4.69%	0.00%	0.83%	0.28%	0.18%	0.10%
2011	446.12	28.03	4.98%	0.00%	0.85%	0.23%	0.18%	0.08%
2012	322.37	25.01	6.06%	0.00%	0.82%	0.55%	0.18%	0.20%
2013	650.48	43.57	5.40%	0.00%	0.72%	0.33%	0.16%	0.12%
2014	706.56	44.14	4.81%	0.00%	0.84%	0.33%	0.18%	0.12%
2015	332.15	26.34	6.17%	0.00%	0.87%	0.55%	0.19%	0.20%
2016	675.35	43.64	5.26%	0.00%	0.77%	0.22%	0.17%	0.08%

Table 4.3 shows the yearly interception contribution regarding different land cover types. On average, the yearly total interception accounts for around 6.5% to 8.5% of total rainfall (25 to 44 mm). Even though the total interception to rainfall ratio was not very high, it can be observed that grass make the largest spatial contribution to the rainfall interception (over 70% of interception for each year during the study period). The large extent of grass (over 70% coverage of the study area) was expected to be the reason for such high interception contribution, as shown in Table 4.2. This indicates the importance of studying grass interception in savannah areas, such as the Sardon catchment, charaterised by sparse occurrence of trees.

In terms of the yearly total interception, small differences were observed among the dry years, as well as the wet years, which are defined in Table 3.2. The interception for dry years ranges from 25 to 26 mm, while the interception for wet years ranges from 42 to 44 mm. This may be due to the limited satellite

images that were retrieved. As only two years (one for dry year and one for wet year) of satellite images were used for deriving vegetation indices, the calculated canopy storage capacity and fractional canopy cover were the same for dry years as well as wet years. Even though the approach of selecting the representative dry year and wet year consider the vegetation development difference under different yearly water supply conditions, there could be vegetation development difference among dry years as well as wet years. In such a case, further investigation of temporal grass interception may be needed.

4.1.2. Potential evapotranspiration

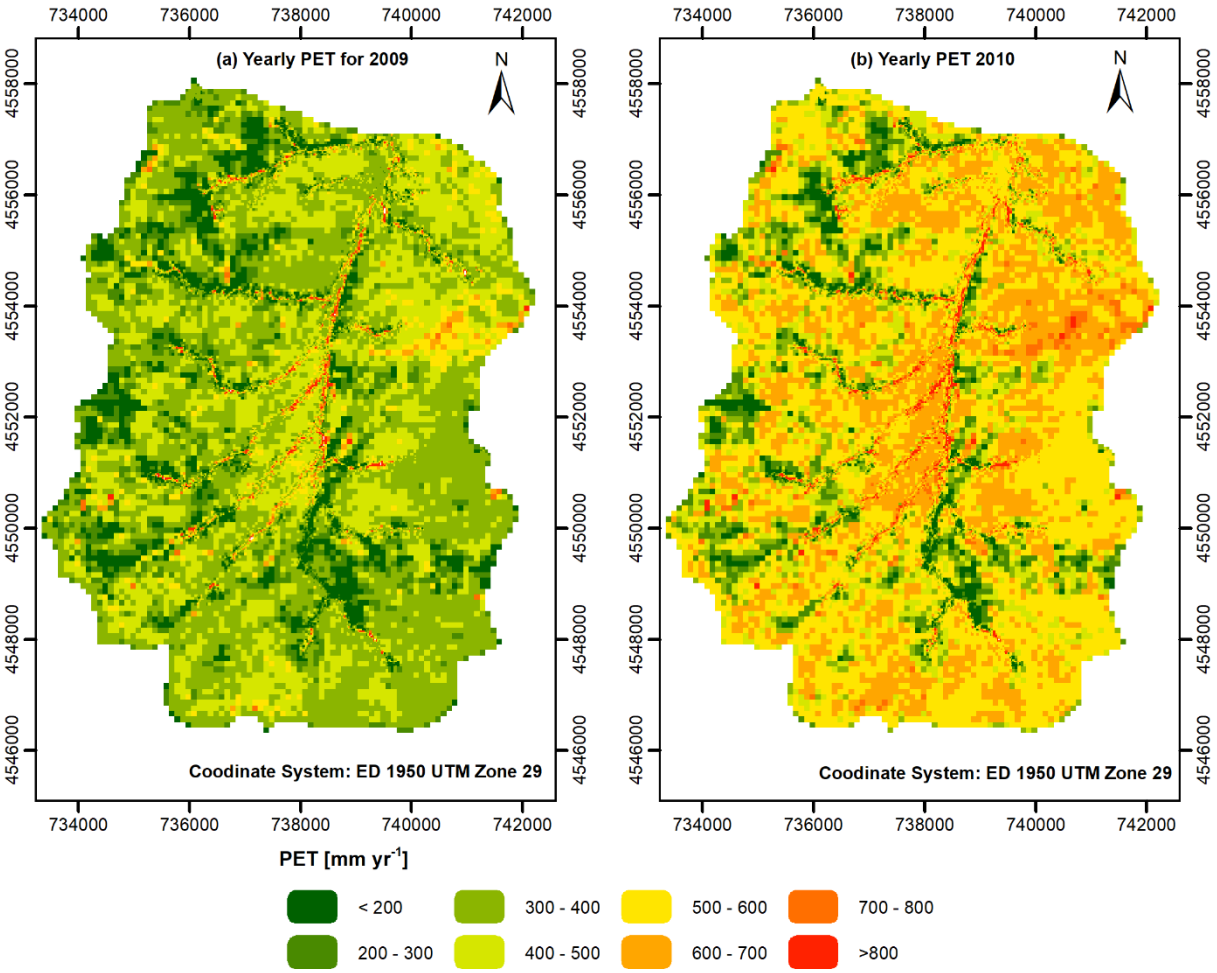

Figure 4.2 Spatial distribution of *PET* in the model grid for different hydrological years.

As shown in Figure 4.2, an obvious year difference of *PET* was observed. In the dry year 2009, the majority of the study area had *PET* values ranging from 300 to 500mm, while *PET* values largely increased to 500 ~ 700 mm for a large area in the wet year 2010. This yearly difference was expected to be attributed to thriving grass in the wet year. Regarding the spatial distribution of *PET* values, low *PET* values (dark green part in Figure 4.2) were observed mainly on the outcrops area, compared with the land cover map (Figure 2.3). Besides, in Figure 4.2 (b), high *PET* values over 800 mm yr^{-1} can be observed along the main Sardon river and streams. This high *PET* value may be due to the presence of sparsely distributed *Q.i* and *Q.p*.

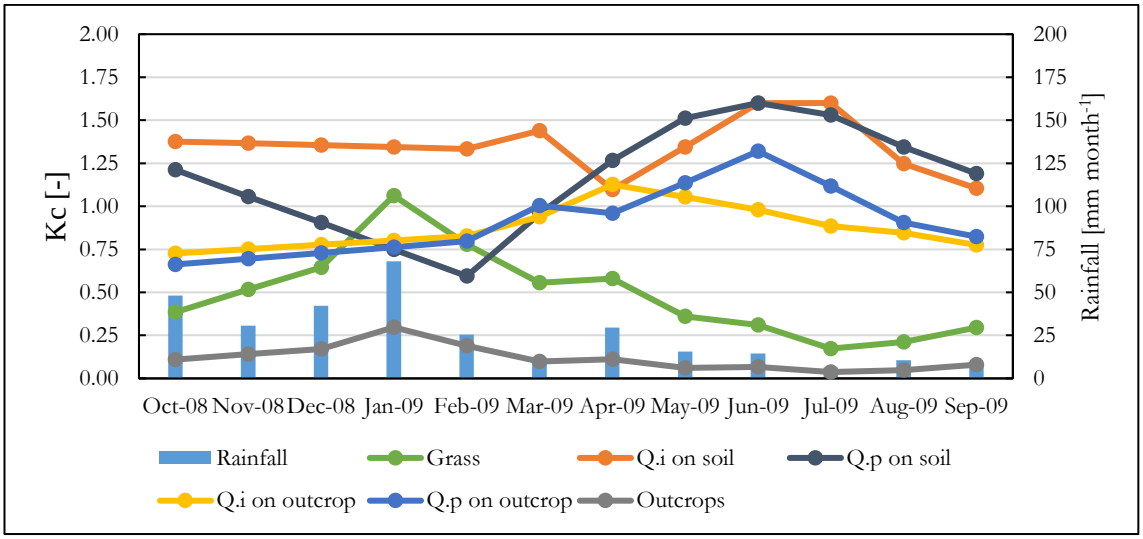

Figure 4.3 Monthly K_c values for the dry year 2009.

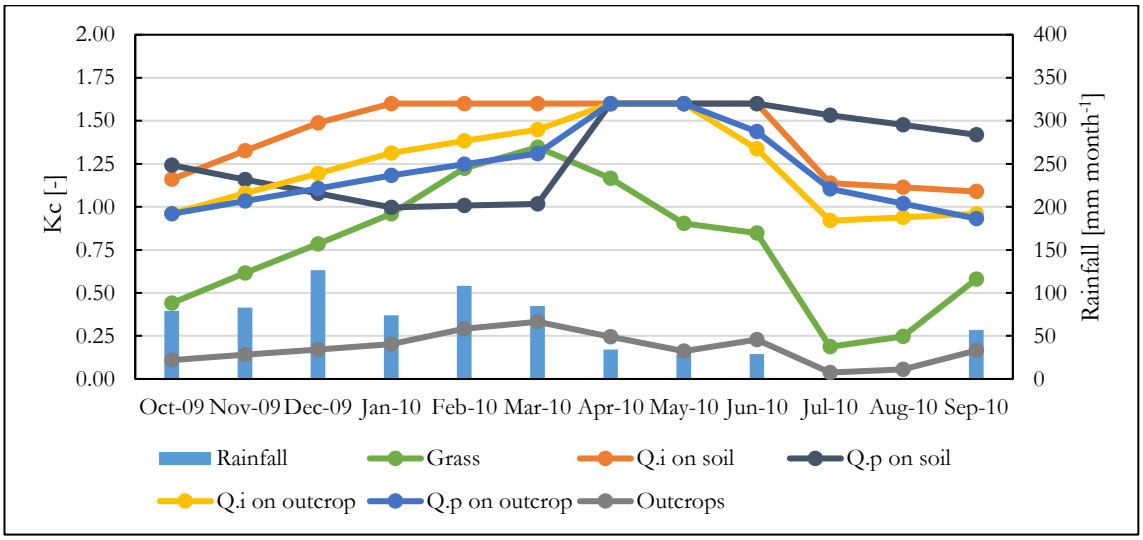

Figure 4.4 Monthly K_c values for the wet year 2010

In general, *Q.i* and *Q.p* have higher K_c values than grass, but grass can temporally have higher K_c values than oak trees when monthly rainfall was high. It was noticed that *Q.p* tends to have lower K_c values than *Q.i* from October to March for both years. As *Q.p* is a type of deciduous tree, the lower K_c values may be due to the deciduous period as mentioned by Hassan et al. (2017), consequently low tree transpiration. However, it was observed that *Q.p* temporally have higher K_c values than *Q.i* from July to August during the dry season, and this matches the study of Reyes-Acosta and Lubczynski (2013). They studied the tree transpiration in the dry season in the Sardon catchment, and they concluded that the averaged transpiration rate of *Q.p* (1.19 mm d^{-1}) was higher than *Q.ilex* (0.83 mm d^{-1}) during the dry season.

The temporal variability of averaged *PET* and ET_o for the entire study area is shown in Figure 4.5. Obvious yearly differences in *PET* can be observed. Wet years have higher *PET* values than dry years (definition of dry and wet years can be found in Table 3.2), which can be attributed to vegetation thriving in wet years. Comparing *PET* with ET_o, *PET* generally was lower than ET_o for the whole study period, and this could be explained by two reasons: i) outcrops cover 21% of the study area but have small

contribution to PET ; ii) grass normally is active only for few months and dormant during most of a hydrological year in the study area.

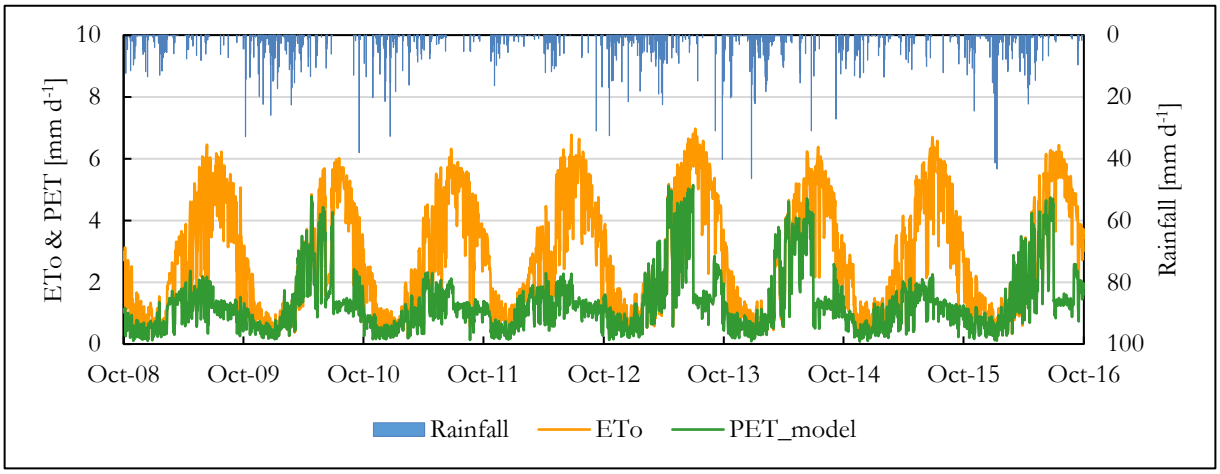

Figure 4.5 Temporal variability of averaged PET and ET_o for the whole study area.

4.2. Model calibration

4.2.1. Calibrated parameters

Table 4.4 shows the calibrated parameters. Both layers have low values of calibrated K_h and K_v, which was expected for the hardrock aquifer. Dewandel et al. (2006) measured the K_h for both saprolite layer and fissured layer in India. In their study, the measured K_h of saprolite layer ranges between 0.008 and 2.6 m d^{-1}, while the measured K_h of fissured layer ranges between 0.00008 m d^{-1}, where the well does not intersect any conductive fissure, and 86.4 m d^{-1}, where the well intersects several conductive fissures. The calibrated K_h values for both layers showed an agreement with the measurements of Dewandel et al. (2006). Besides, the calibrated S_y and S_s showed generally low values, which were expected for HRSs. The spatial distributions of K_h , K_v , S_y and S_s are shown in Figure 4.6, Figure 4.7, Figure 4.8 and Figure 4.9, respectively.

Table 4.4 Calibrated parameters

Parameter		Value range	Unit	Model package
K_h	Horizontal hydraulic conductivity	0.02 ~ 3	[m d^{-1}]	NPF
K_v	Vertical hydraulic conductivity	0.0005 ~ 0.07	[m d^{-1}]	NPF
K_{sat}	Vertical saturated hydraulic conductivity	0.0005 ~ 0.07	[m d^{-1}]	UZF
K_v	Streambed hydraulic conductivity	0.0005 ~ 0.07	[m d^{-1}]	SFR
K_d	Drain bed hydraulic conductivity	0.0005 ~ 0.07	[m d^{-1}]	DRN
C_d	Drain bed conductance	2.25 ~ 405	[m^2 d^{-1}]	DRN
S_y	Specific yield	0.001 ~ 0.08	[-]	STO
S_s	Specific storage	10^{-6} ~ 10^{-5}	[m^{-1}]	STO
α	MVR factor	0.5 ~ 0.85	[-]	UZF

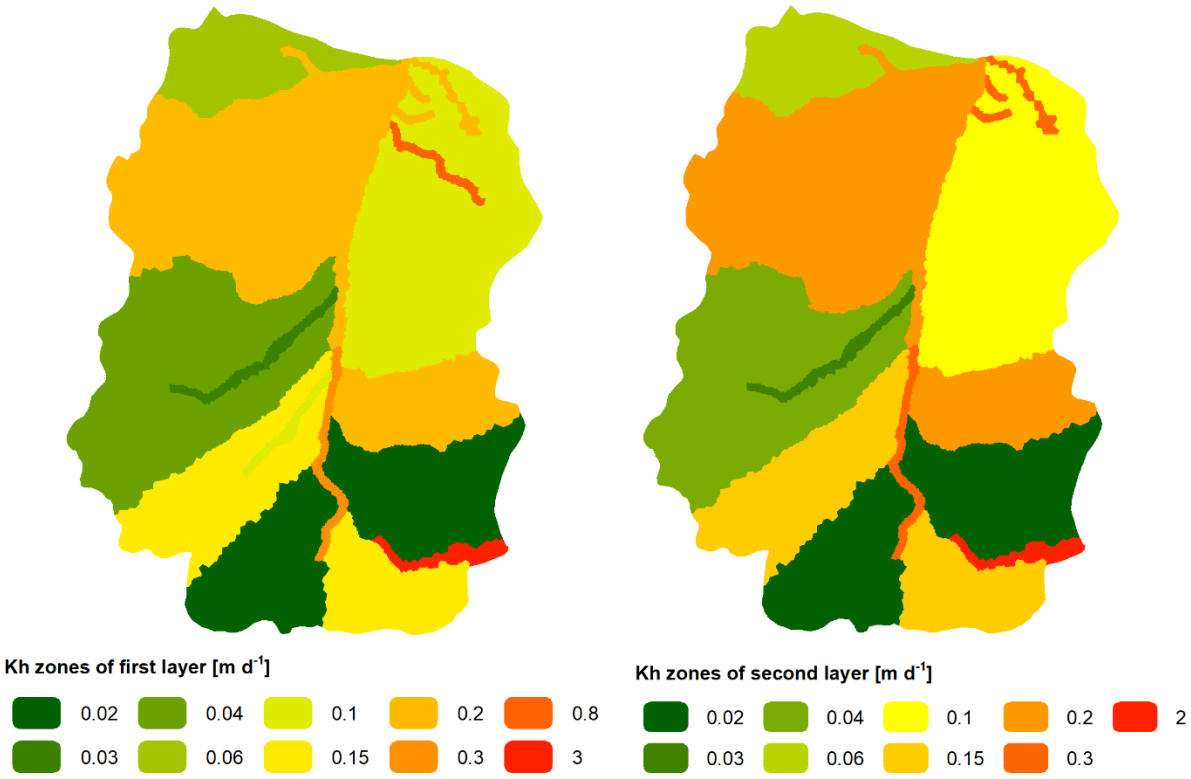

Figure 4.6 Spatial distribution of K_h

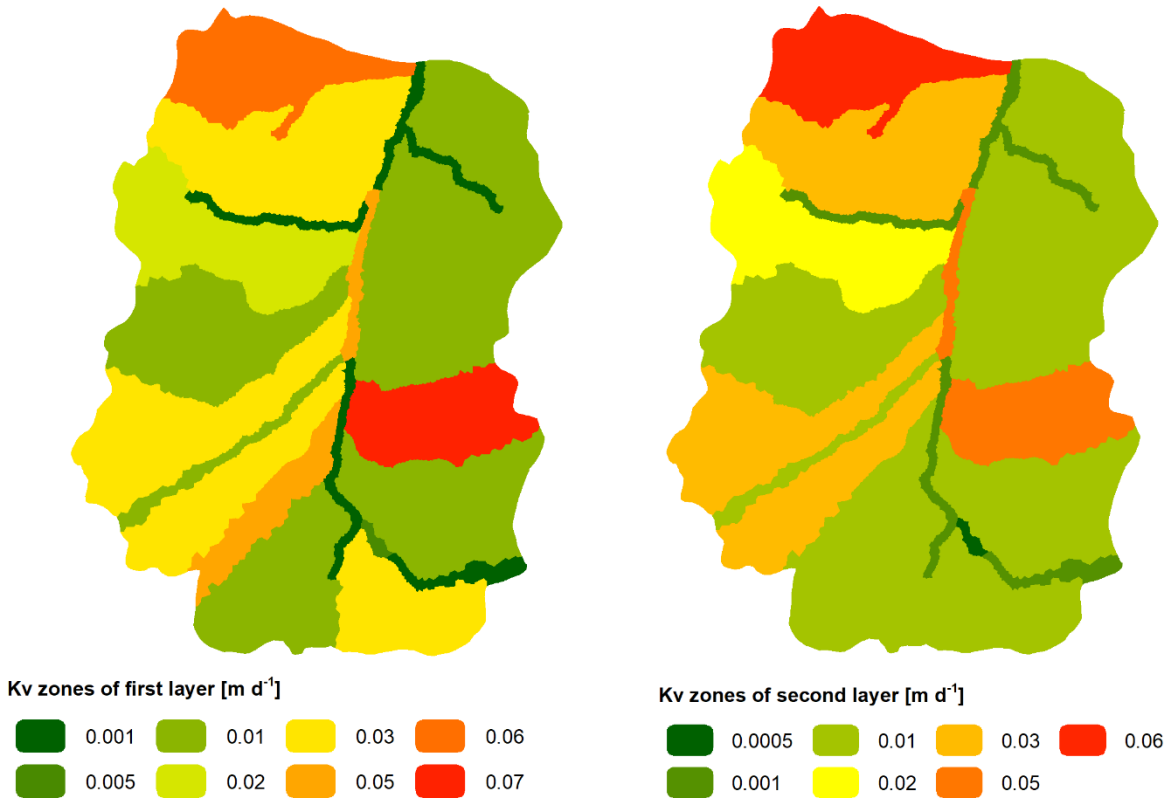

Figure 4.7 Spatial distribution of K_v

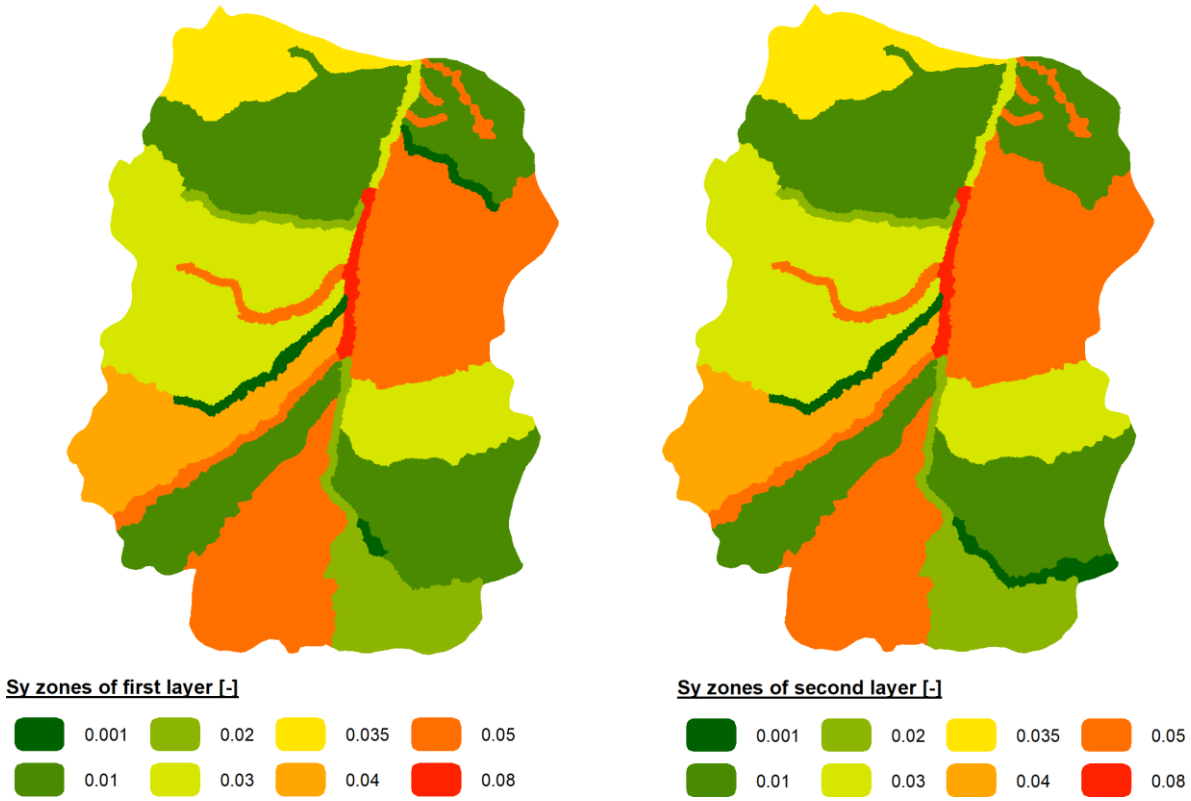

Figure 4.8 Spatial distribution of S_y

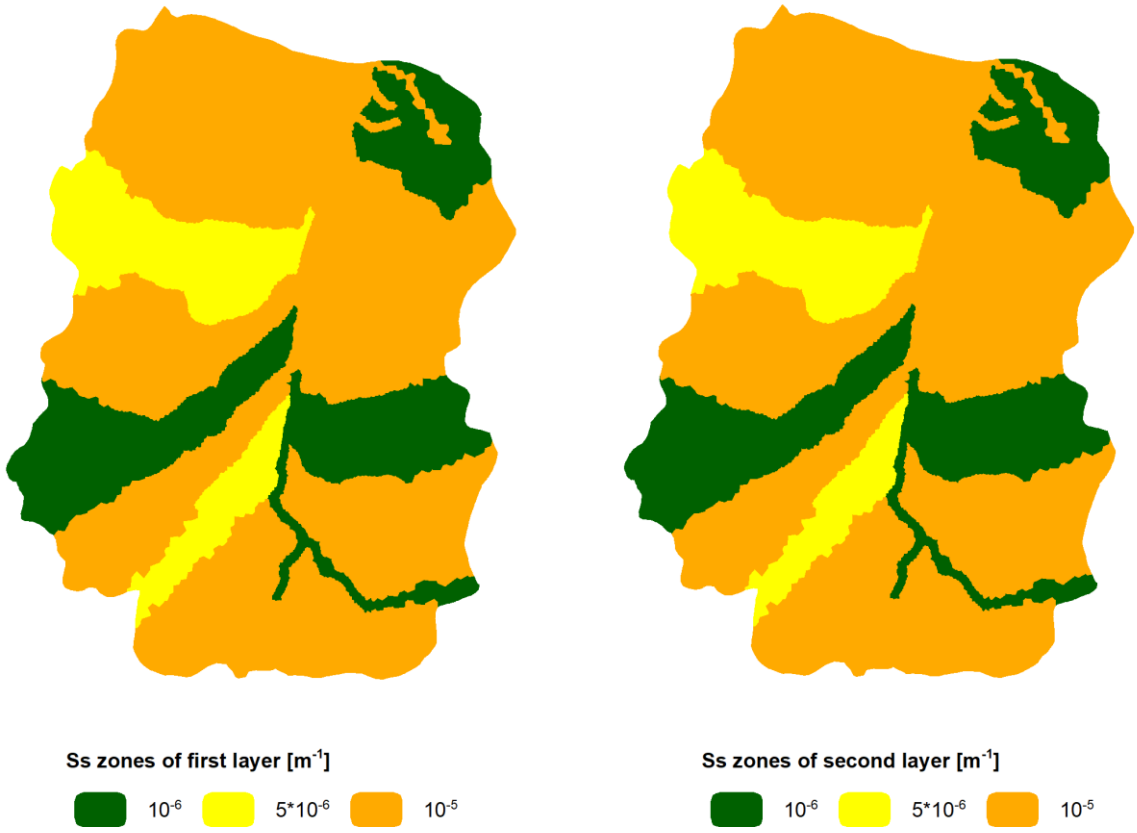

Figure 4.9 Spatial distribution of S_s

4.2.2. Calibrated heads

As shown in Table 4.5, total 11 sites were well-calibrated with *RMSE* less than 1 m for the entire simulation period (October 2008 to September 2016). Even though PGB0 and PGJ0 have RMSE around 1.3 m, good patterns of simulated heads against observed heads were observed in Figure 4.11.

Table 4.5 Statistical summary of head calibration in 13 sites

Observation sites	MAE [m]	RMSE [m]	Number of daily records
PGJTM0	0.41	0.59	293
PMU1	0.63	0.72	1282
PMU3	0.78	0.87	425
PPN0	0.33	0.44	790
PTB2	0.51	0.70	1330
PTM1	0.63	0.74	655
W1_PCL7	0.41	0.49	2201
W1_PN	0.57	0.69	2196
W1_SD	0.56	0.72	2200
W1_TB	0.29	0.35	2198
W2_PCL7	0.44	0.53	2194
PGB0	0.91	1.32	2374
PGJ0	1.09	1.22	2575

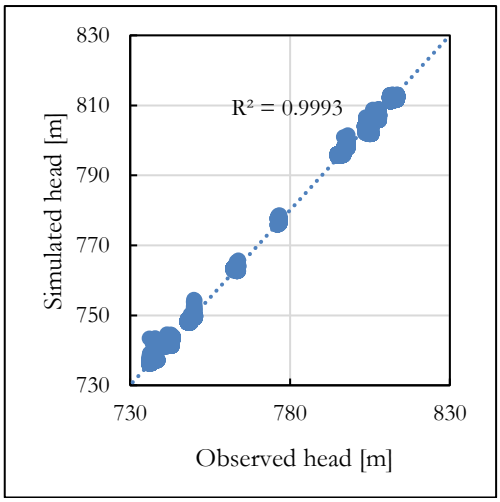

Figure 4.10 Scatter plot of daily observed heads and simulated heads of 13 sites

As shown in Figure 4.10, the scatter plot shows a high agreement ($R^2 > 0.9$) between observed heads and simulated heads.

The comparison of simulated heads and observed heads in 13 observation sites are shown in Figure 4.11. Generally, the simulated heads follow the temporal patterns of the observed heads, but some obvious discrepancies between simulated and observed heads can be observed. These discrepancies could be due to the following reasons: i) errors in the conceptual model, for example, layer thickness; ii) errors in the assignment of hydraulic parameters and storage parameters; iii) errors in spatial heterogeneity representation by relative coarse grid size, compared with point observations; iv) errors in driving forces calculation.

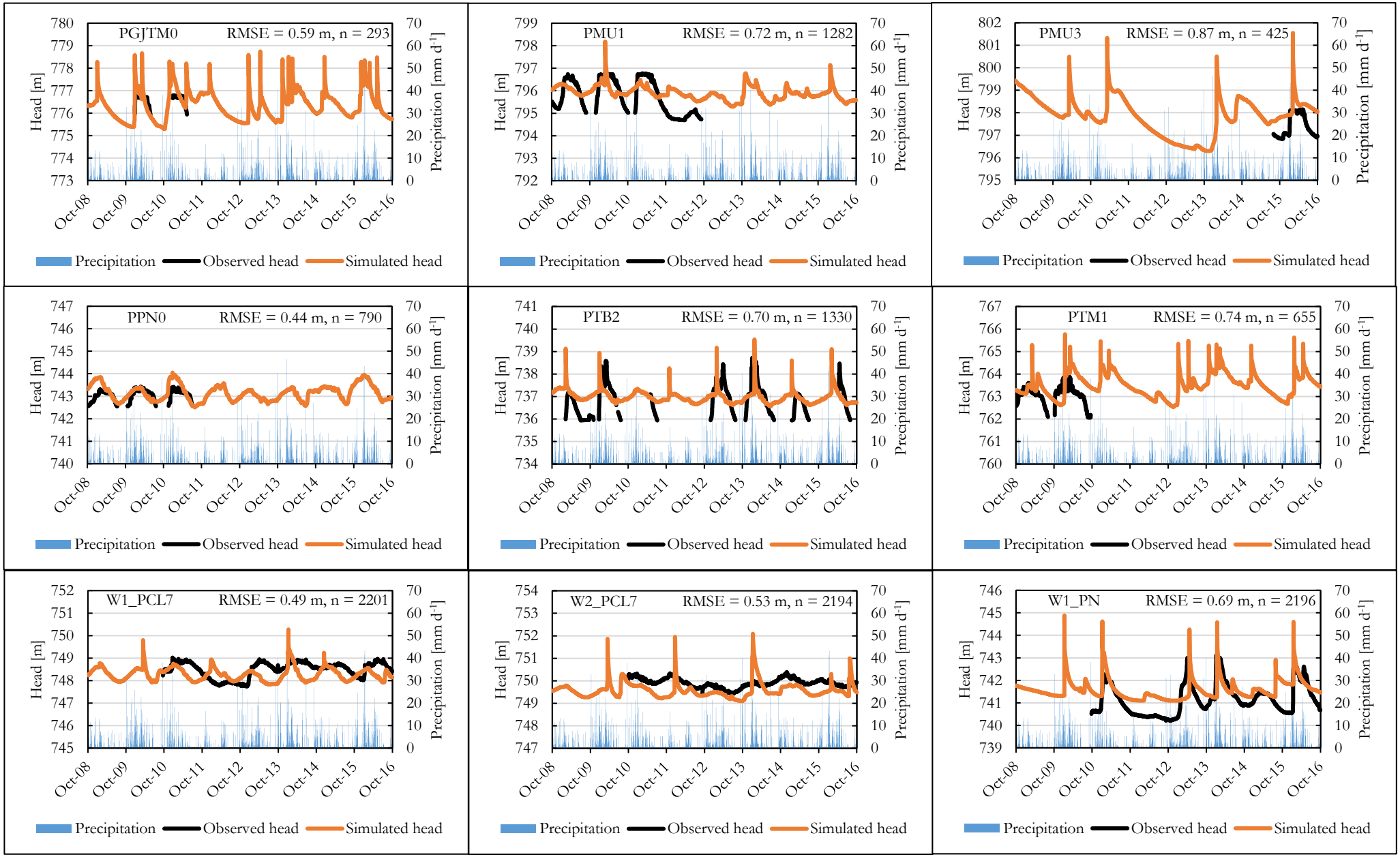
PGJTM0 RMSE = 0.59 m, n = 293
PMU1 RMSE = 0.72 m, n = 1282
PMU3 RMSE = 0.87 m, n = 425
PPN0 RMSE = 0.44 m, n = 790
PTB2 RMSE = 0.70 m, n = 1330
PTM1 RMSE = 0.74 m, n = 655
W1_PCL7 RMSE = 0.49 m, n = 2201
W2_PCL7 RMSE = 0.53 m, n = 2194
W1_PN RMSE = 0.69 m, n = 2196
Head [m]
Precipitation [mm d-1]
Oct-08
Oct-09
Oct-10
Oct-11
Oct-12
Oct-13
Oct-14
Oct-15
Oct-16
Precipitation
Observed head
Simulated head

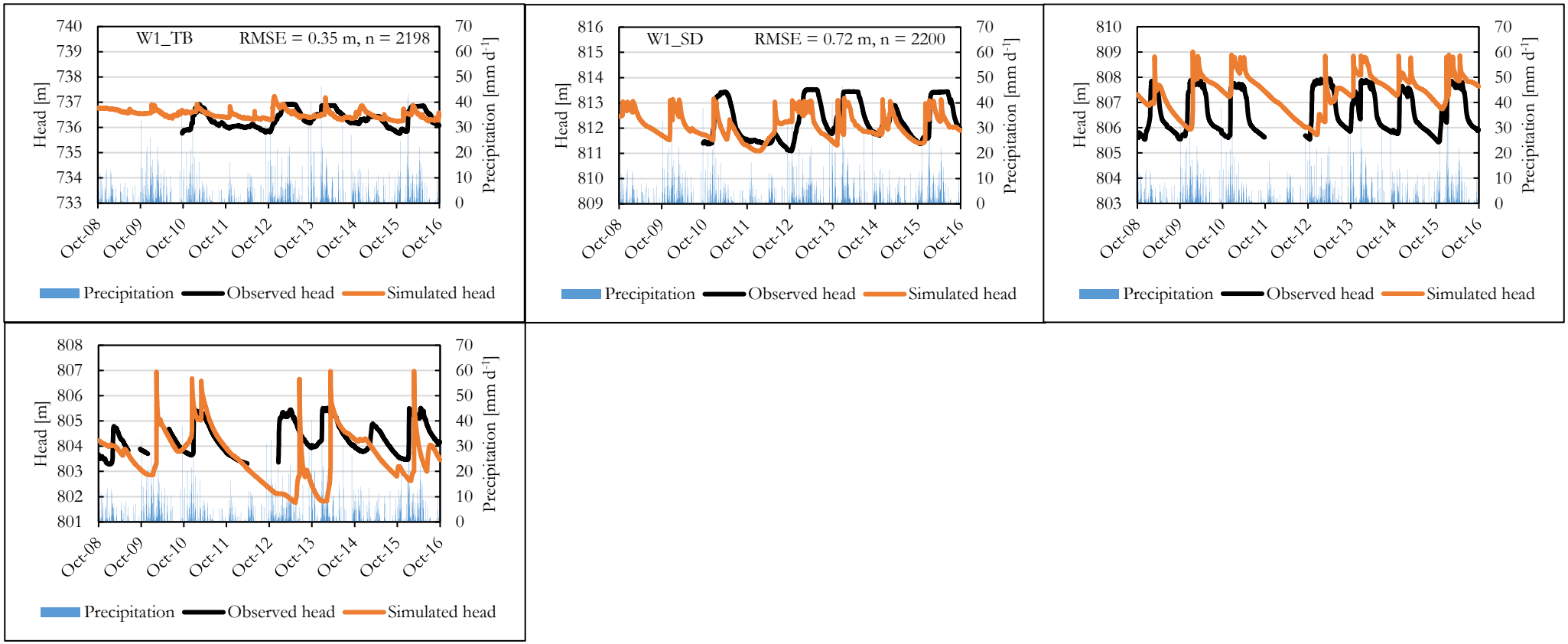

Figure 4.11 Simulated heads and observed heads for 13 observation sites from 1 October 2008 to 30 September 2016 (the locations of observation sites were shown in Figure 2.1)

4.2.3. Calibrated evapotranspiration

The comparison between simulated ET and MODIS ET is shown in Table 4.6 and Figure 4.12. Overall, the simulated ET shows a good match with MODIS ET as the percentage differences for all years were within ±15%. The yearly ET underestimation ranges from 7 to 29 mm, while the yearly ET overestimation ranges from 2 to 52 mm.

As shown in Table 4.6, uniform MVR factors were applied for both dry years ($\alpha = 0.5$) and wet years ($\alpha = 0.85$), and this approach resulted in acceptable yearly difference (<15%), which may indicate the validity of similar distribution portion of RI and Exf_{gw} to the streams in dry years and in wet years. For dry years, 50% of RI and Exf_{gw} were transferred to the streams, while for wet years, 85% of RI and Exf_{gw} were transferred to the streams.

Table 4.6 Statistics of yearly simulated ET from the model and MODIS ET.

Year	Rainfall [mm/yr]	Simulated ET [mm/yr]	MODIS ET [mm/yr]	Difference [mm]	Difference [%]	MVR factor (α) [-]
2009	311	277	306	-29	-9.48%	0.5
2010	703	405	402	2	0.55%	0.85
2011	446	350	382	-32	-8.44%	0.5
2012	322	286	300	-14	-4.55%	0.5
2013	650	454	402	52	12.98%	0.85
2014	707	416	400	16	4.00%	0.85
2015	332	339	346	-7	-2.16%	0.5
2016	675	453	435	18	4.08%	0.85

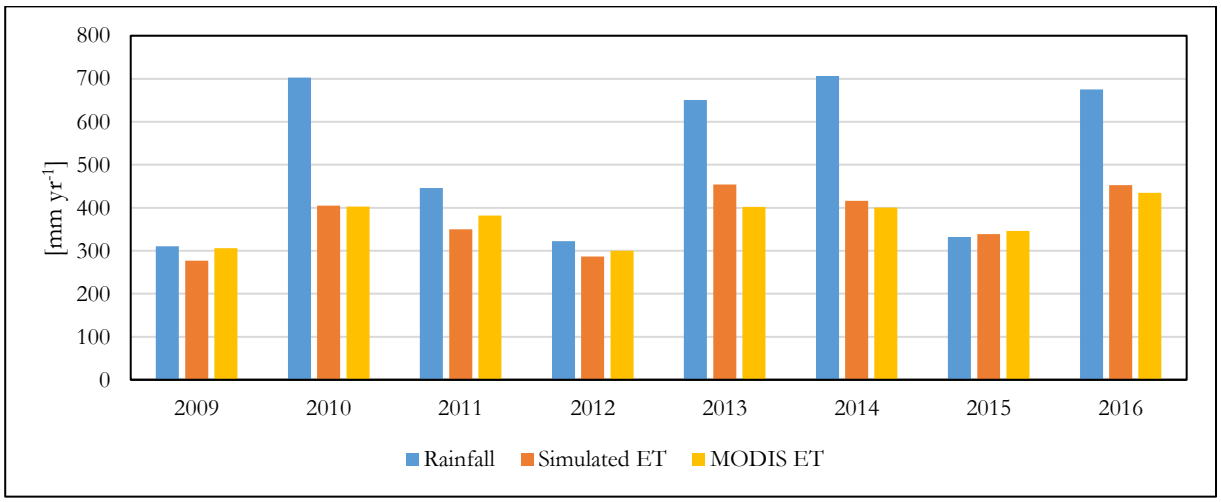

Figure 4.12 Yearly simulated ET and MODIS ET

From Figure 4.12, it can be observed that the ratio of simulated ET to rainfall was generally high. In dry years, over 80% of rainfall was evapotranspired, while simulated ET accounted for over 50% of rainfall in wet years. The large amount of ET may indicate the aridity of the Sardon catchemt, which is a typical water limited environment.

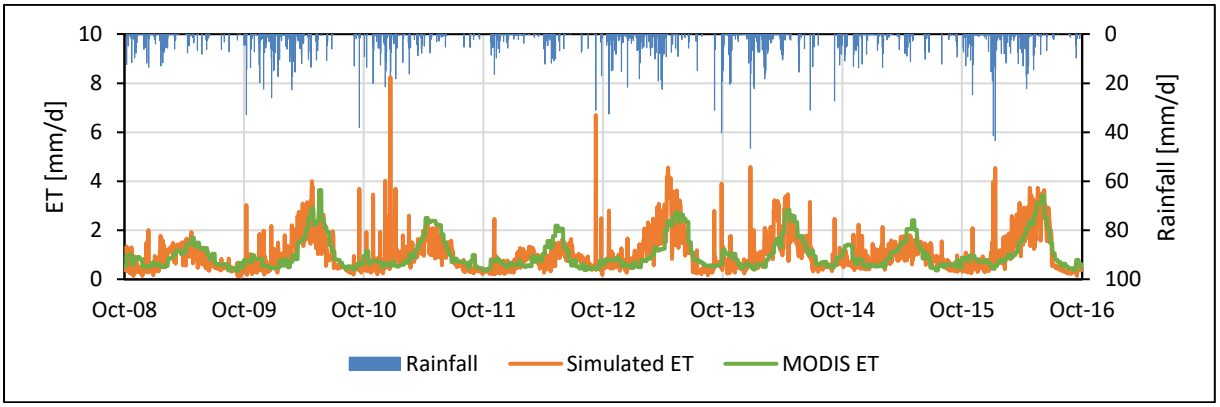

Figure 4.13 Daily simulated ET and MODIS ET

Even though the model was calibrated by yearly MODIS ET, daily simulated ***ET*** surprisingly showed a good match (RMSE = 0.57mm) with daily MODIS ET, as shown in Figure 4.13. This good match may indicate that calibrating the model with yearly MODIS ET was sufficient.

The main differences between simulated ***ET*** and MODIS ET can be observed for rainy days. The simulated ***ET*** had significant responses to rainfall, while MODIS ET showed gentle increases. By checking the components of simulated ***ET*** as shown in Eq. (3-3), the sudden increases of simulated ET were mainly attributed to a large amount of rejected infiltration evapotranspired (RI^e) resulting from heavy rainfall. This may indicate the capacity of IHM for a realistic simulation.

4.3. Comparison with selected satellite soil moisture product

Figure 4.14 shows the simulated soil moisture at 5 cm depth and SSM1km from 1 January 2015 to 30 September 2016. Total 119 daily satellite soil moisture observations were retrieved.

Overall, simulated soil moisture and satellite soil moisture showed an acceptable match, with RMSE = 0.081 m^3 m^{-3} and Pearson correlation = 0.65. Similar trends for both simulated and satellite soil moisture can be observed. Simulated soil moisture and satellite soil moisture showed increases to rainfall events and decreases to dry periods. In general, the magnitude of simulated soil moisture was close to satellite soil moisture, but satellite soil moisture showed more significant fluctuations. Satellite soil moisture ranges from 0.018 to 0.400 m^3 m^{-3}, while simulated soil moisture ranges from 0.083 to 0.395 m^3 m^{-3}.

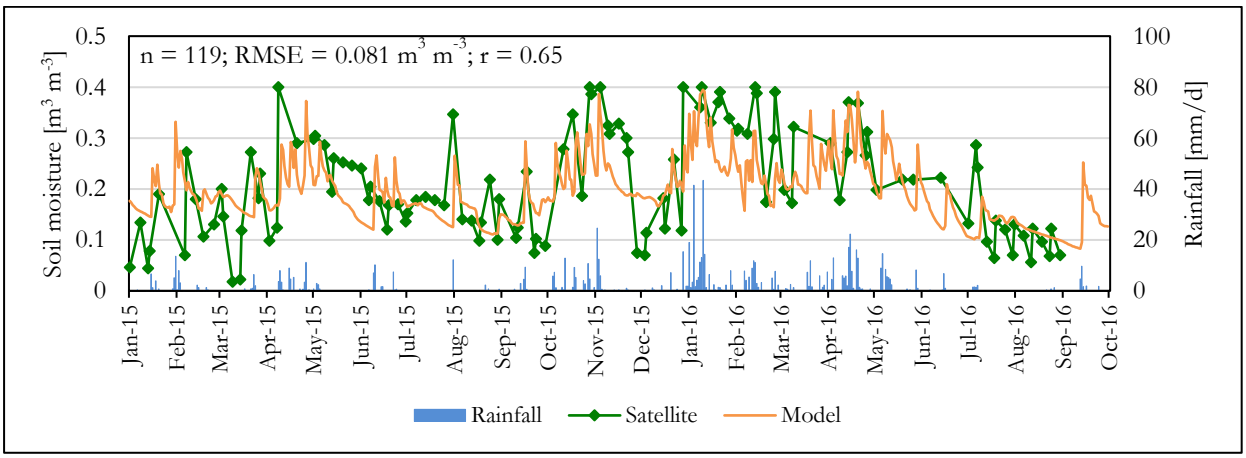

Figure 4.14 Daily simulated soil moisture at 5 cm depth and SSM1km

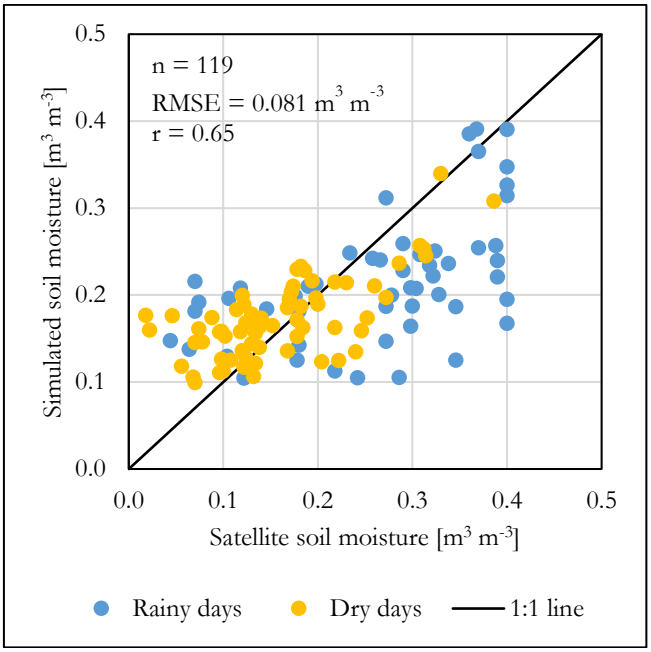

Figure 4.15 Scatter plot of simulated and satellite soil moisture

Table 4.7 Statistics summary of simulated and satellite soil moisture

Type	Number of days	RMSE [m^3 m^{-3}]	r [-]
Rainy days	53	0.102	0.54
Dry days	66	0.057	0.69
Overall	119	0.081	0.65

Figure 4.15 shows the scatter plot simulated and satellite soil moisture. By splitting the data into rainy days and dry days (no rainfall), differences can be observed in terms of simulated and satellite soil moisture.

In rainy days, satellite soil moisture generally showed higher values than simulated soil moisture. In dry days, simulated soil moisture was either higher or lower than satellite soil moisture. For soil moisture below 0.2 m^3 m^{-3}, simulated soil moisture tended to have higher values than satellite soil moisture, while for soil moisture above 0.2 m^3 m^{-3}, simulated soil moisture was generally lower than satellite soil moisture.

In general, simulated and satellite soil moisture showed better agreement in dry days (RMSE = 0.057 m^3 m^{-3}, r = 0.69) than in rainy days (RMSE = 0.102 m^3 m^{-3}, r = 0.54).

4.4. Water balance

The hydrological system in this study was characterised as two zones: i) land surface and unsaturated zone; ii) groundwater zone. Daily rates of each hydrological component were extracted from the output files of MODFLOW 6, and then summed to yearly rates in order to have an insight into the yearly water balance for the whole simulation period (2009 ~ 2016), as shown in Table 4.8 and Table 4.9. Each hydrological component and the water balance equations are referred to Section 3.3.4.

For the 8-year mean water balance of the whole system, the main input is P (518.28 mm yr^{-1}), while the outputs consist of ET (72% of P), q (26% of P) and negligible q_g (0.1% of P). It can be observed that the main output of the catchment was ET, which was substantially higher than q, and this was expected as the streams flow intermittently in the semi-arid Sardon catchment. The ET is comprised of two surface components: E_{sf} (9.4% of ET) and RI^e (4.8% of ET), and the tree subsurface components: ET_u (71.4% of ET), ET_g (7.6% of ET) and Exf_{gw}^e (6.8% of ET). E_{sf} was the main surface contribution to the total ET, while ET_u was the main subsurface contribution. Besides, it was noticed that subsurface components made a substantial contribution (86%) to the total ET. The q is comprised of RI^s (43% of q), Exf_{gw}^s (47% of q) and q_B (10% of q). The sum of RI^s and Exf_{gw}^s represents the total overland flow (90% of q), which was significantly higher than q_B. This may indicate the intermittent streams in the Sardon catchment were highly affected by the overland flow process.

For the land surface and unsaturated zone, the main input is P_e (93.3% of P), while the main outputs are ET_u (55% of P_e), R_g (24.8% of P_e) and RI (15.8% of P_e). The high P_e was expected because of the sparsely distributed oak trees (*Q.i* and *Q.p*) and seasonal grass. The high contribution of ET_u may indicate the importance of applying IHM in a WLE-HRS system as the Sardon catchment, because the unsaturated zone fluxes were expected to highly affect the recharge to the groundwater zone. The 8-year mean ΔS_u was 21.2 mm yr^{-1} (4.1% of P), which means the unsaturated zone received recharge during the simulation period.

For the groundwater zone, the main input are R_g (23.1% of P) and negligible q_{sg} (0.5% of P), while the outputs are Exf_{gw} (74.4% of R_g), ET_g (23.7% of R_g) and q_{gs} (13.3% of R_g). The significant amount of Exf_{gw} indicates the surface-groundwater interactions in the Sardon catchment because of the shallow water table and low storativity. It was noticed that the 8-year mean ΔS_g was -11.5 mm yr^{-1} (2.3% of P), which means the groundwater zone generally lost storage over the simulation period.

Table 4.8 Yearly water balance of each hydrological component. The unit is mm yr^{-1}.

Year	P	E_{sf}	P_e	ET	ET_u	ET_g	RI	RI^e	RI^s	Exf_{gw}	Exf^e_{gw}	Exf^s_{gw}	q	q_B	q_{gs}	q_{sg}	q_g	R_g	R_n	ΔS_u	ΔS_g	ΔS
2009	310.53	25.81	284.71	276.70	193.03	28.41	25.77	12.89	12.89	33.12	16.56	16.56	44.27	14.82	16.86	2.04	0.89	33.36	-28.17	32.26	-43.89	-11.63
2010	702.69	42.39	660.30	404.65	293.32	34.37	119.46	17.92	101.54	110.97	16.65	94.33	209.88	14.01	16.76	2.74	0.84	145.36	0.02	101.82	-14.84	86.98
2011	446.12	28.03	418.09	349.63	214.05	28.11	65.70	32.85	32.85	93.17	46.59	46.58	92.33	12.91	15.25	2.35	0.78	121.37	0.09	16.69	-13.60	3.09
2012	322.37	25.01	297.36	286.36	201.78	21.09	30.50	15.25	15.25	46.46	23.23	23.23	50.05	11.57	13.66	2.08	0.80	65.57	-1.98	-0.85	-14.35	-15.21
2013	650.48	43.57	606.91	454.03	354.50	28.39	106.05	15.91	90.14	77.74	11.66	66.07	168.34	12.12	14.64	2.52	0.78	107.88	1.75	38.07	-11.16	26.92
2014	706.56	44.14	662.42	416.36	302.58	30.76	126.74	19.01	107.73	132.43	19.86	112.57	234.64	14.34	17.16	2.82	0.82	182.22	19.03	50.52	3.86	54.38
2015	332.15	26.34	305.81	338.63	225.50	23.26	23.63	11.82	11.82	103.41	51.71	51.71	78.47	14.95	17.28	2.34	0.81	145.24	18.57	-88.90	2.81	-86.09
2016	675.35	43.64	631.71	452.76	342.11	32.74	113.25	16.99	96.26	115.22	17.28	97.94	207.58	13.38	16.13	2.75	0.74	156.47	8.50	19.77	-5.63	14.14
Mean	518.28	34.87	483.41	372.39	265.86	28.39	76.39	17.83	58.56	89.07	25.44	63.62	135.70	13.51	15.97	2.45	0.81	119.68	2.23	21.17	-12.10	9.07
Min	310.53	25.01	284.71	276.70	193.03	21.09	23.63	11.82	11.82	33.12	11.66	16.56	44.27	11.57	13.66	2.04	0.74	33.36	-28.17	-88.90	-43.89	-86.09
Max	706.56	44.14	662.42	454.03	354.50	34.37	126.74	32.85	107.73	132.43	51.71	112.57	234.64	14.95	17.28	2.82	0.89	182.22	19.03	101.82	3.86	86.98

Table 4.9 Mean water balance for the total simulation period (2009 ~ 2016) for each zone. Positive values stand for inputs to the zone, while negative values represent outputs from the zone. The unit is mm yr^{-1}.

Zone	P	P_e	ET	ET_u	ET_g	RI	Exf_{gw}	q	q_{gs}	q_{sg}	q_g	R_g	ΔS_u	ΔS_g	ΔS	In	Out	In - out	Discrepancy
Land surface and unsaturated zone		483.41		-265.86		-76.39						-119.68	-21.17			483.41	-483.10	0.31	0.03%
Groundwater zone					-28.39		-89.07		-15.97	2.45	-0.81	119.68		12.10		134.24	-134.23	0.01	0.00%
Entire catchment	518.28		-372.39					-135.70			-0.81				-9.07	518.28	-517.97	-0.32	-0.03%

4.5. Spatial distribution of fluxes

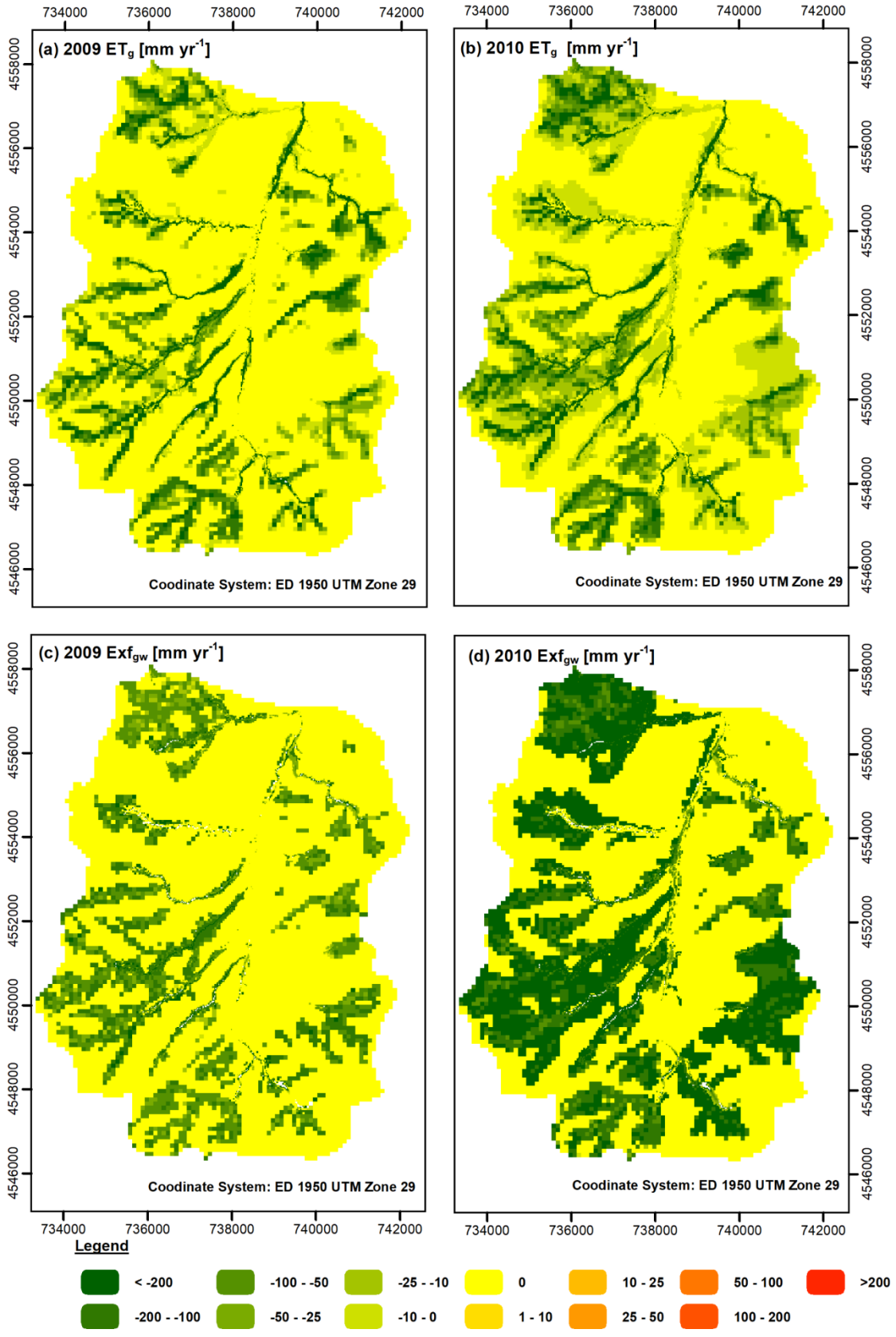

Figure 4.16 Spatial distribution of groundwater evapotranspiration and exfiltration for hydrological year 2009 and 2010.

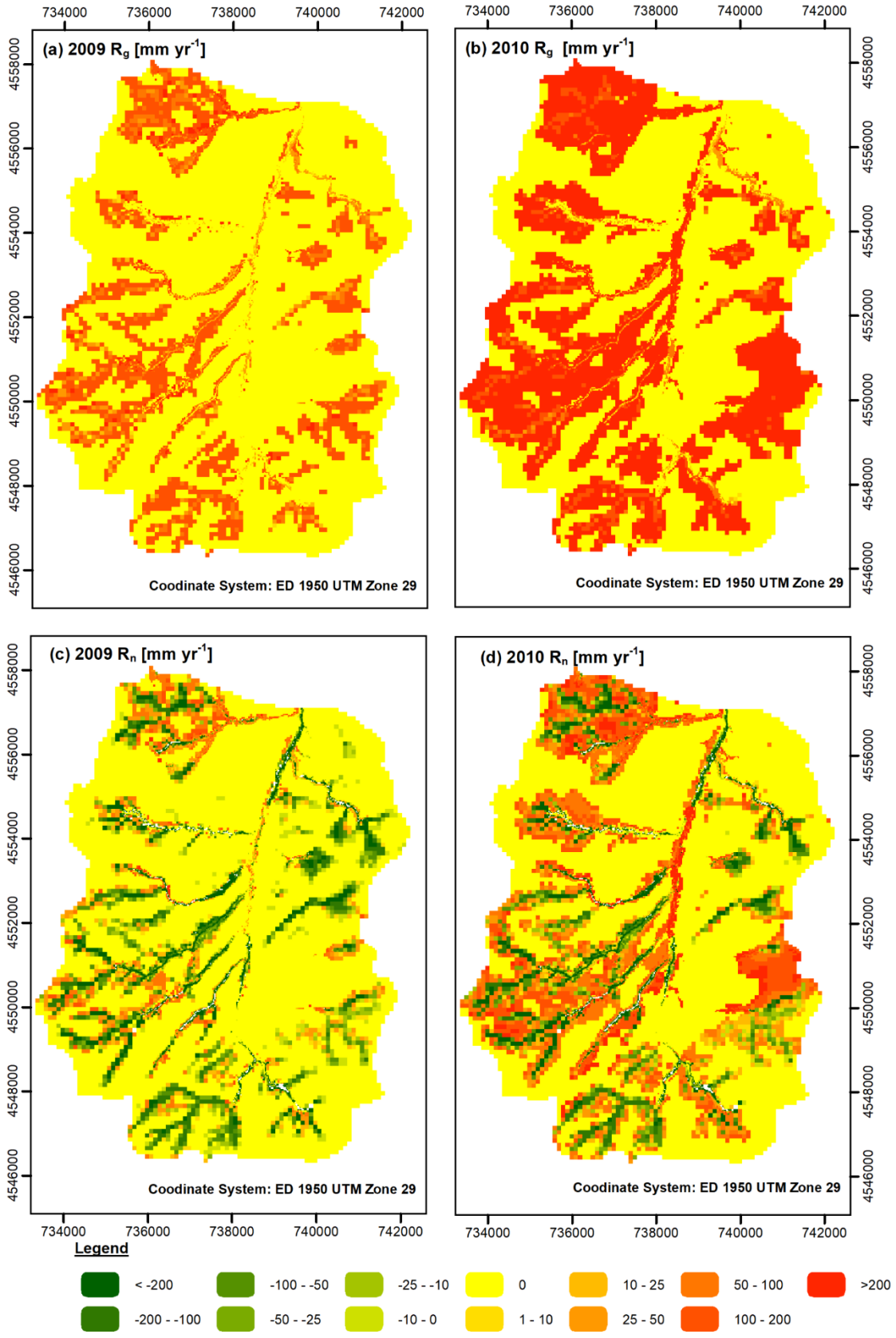

Figure 4.17 Spatial distribution of groundwater gross recharge and net recharge for hydrological year 2009 and 2010.

Spatial distribution of main groundwater zone fluxes is presented for two contrasting hydrological years: the dry year 2009 (P = 310.5 mm) and the wet year 2010 (P = 702.7 mm) as shown in Figure 4.16 and Figure 4.17.

The main outputs are groundwater evapotranspiration (ET_g) and groundwater exfiltration (Exf_{gw}). Both ET_g and Exf_{gw} showed a larger extent in the wet year than in the dry year. This was expected because higher precipitation in the wet year would result in a shallow water table, which allows ET_g and Exf_{gw} to occur. It can be observed that ET_g and Exf_{gw} mostly occurred around the streams, and this could be explained by the shallow water table around streams and the existence of oak trees (*Q.i* and *Q.p*), which have higher extinction depth than grass.

The main input for the groundwater zone is groundwater gross recharge (R_g). For both years, R_g showed high values in the western and southern parts of the catchment. ET_g and Exf_{gw} generally followed the same pattern as R_g, which was expected. For the groundwater net recharge (R_n), it can be observed (Figure 4.17) that negative R_n areas were mostly around the streams in the dry year 2009 and the wet year 2010, but with much larger extent in the dry year. Besides, it was noticed that there were considerable areas with zero R_n in both dry year 2009 and wet year 2010, mainly in the eastern and northwestern parts. The large areas with zero R_n were in agreement with 8-year mean groundwater zone storage lost, as mentioned in Section 4.4.

4.6. Temporal variability of groundwater fluxes

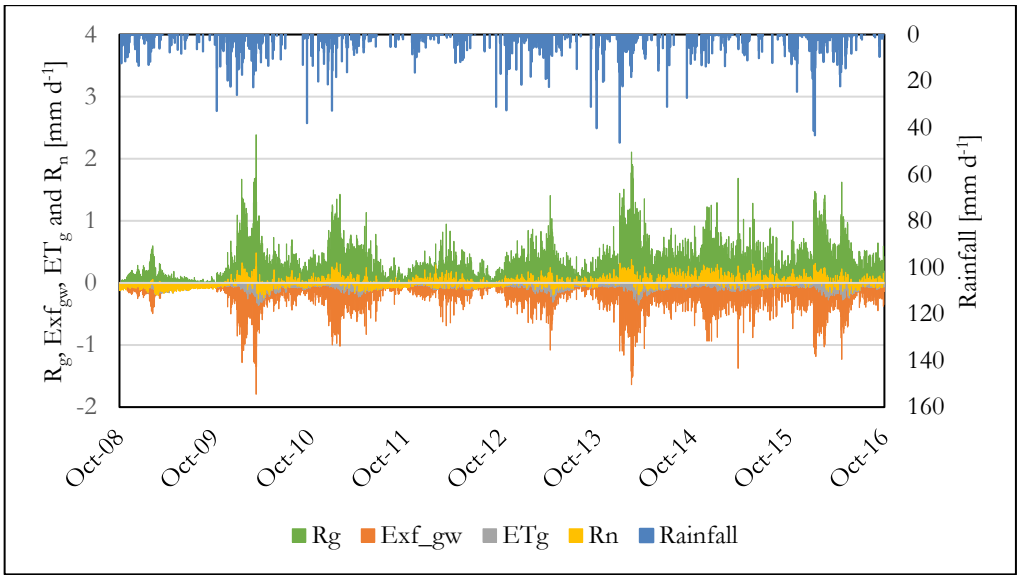

Figure 4.18 Groundwater zone fluxes of 8 hydrological years (2009 ~ 2016)

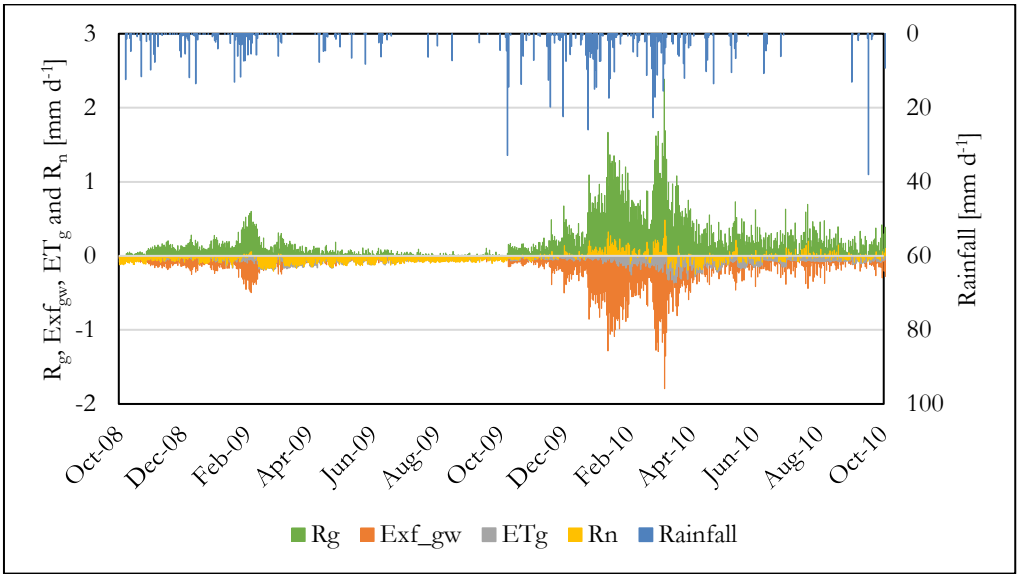

Figure 4.19 Groundwater zone fluxes of the dry year 2009 and the wet year 2010.

The groundwater zone fluxes of 8 hydrological years (2009 ~ 2016) are shown in Figure 4.18. The 8-year daily mean values for different fluxes: R_g (0.33 mm d^{-1}), Exf_{gw} (-0.24 mm d^{-1}) and ET_g (-0.08 mm d^{-1}). As large portion of R_g was lost out of the groundwater zone by Exf_{gw} and ET_g, consequently the mean daily value of R_n was low (0.01 mm d^{-1}).

For the dry year 2009 and the wet year 2010, the groundwater zone fluxes are shown in Figure 4.19. For the dry year 2009, low daily mean values of different fluxes can be observed: R_g (0.09 mm d^{-1}), Exf_{gw} (-0.09 mm d^{-1}), ET_g (-0.08 mm d^{-1}), and this resulted in negative R_n (-0.08 mm d^{-1}) representing discharge conditions. For wet year 2010, daily mean values of different fluxes can be observed: high R_g (0.40 mm d^{-1}), high Exf_{gw} (-0.30 mm d^{-1}), average ET_g (-0.09 mm d^{-1}), and this resulted in low positive R_n (0.01 mm d^{-1}) representing recharge conditions.

4.7. Sensitivity analysis

The sensitivity analysis was performed for testing the response of simulated head to the change of horizontal hydraulic conductivity (K_h), vertical hydraulic conductivity (K_v), specific yield (S_y) and specific storage (S_s).

From Figure 4.20, it can be observed that the model solution was sensitive to K_h, K_v and S_y, while the model solution was insensitive to the change of S_s. For K_h, 50% increase in parameter resulted in 61% increase in overall RMSE, while 50% decrease in parameter resulted in 34% increase in overall RMSE. For K_v, 50% increase led to 30% increase in overall RMSE and 50% decrease resulted in 40% increase in overall RMSE. Regarding S_y, 50% increase can even result in 83% increase in overall RMSE.

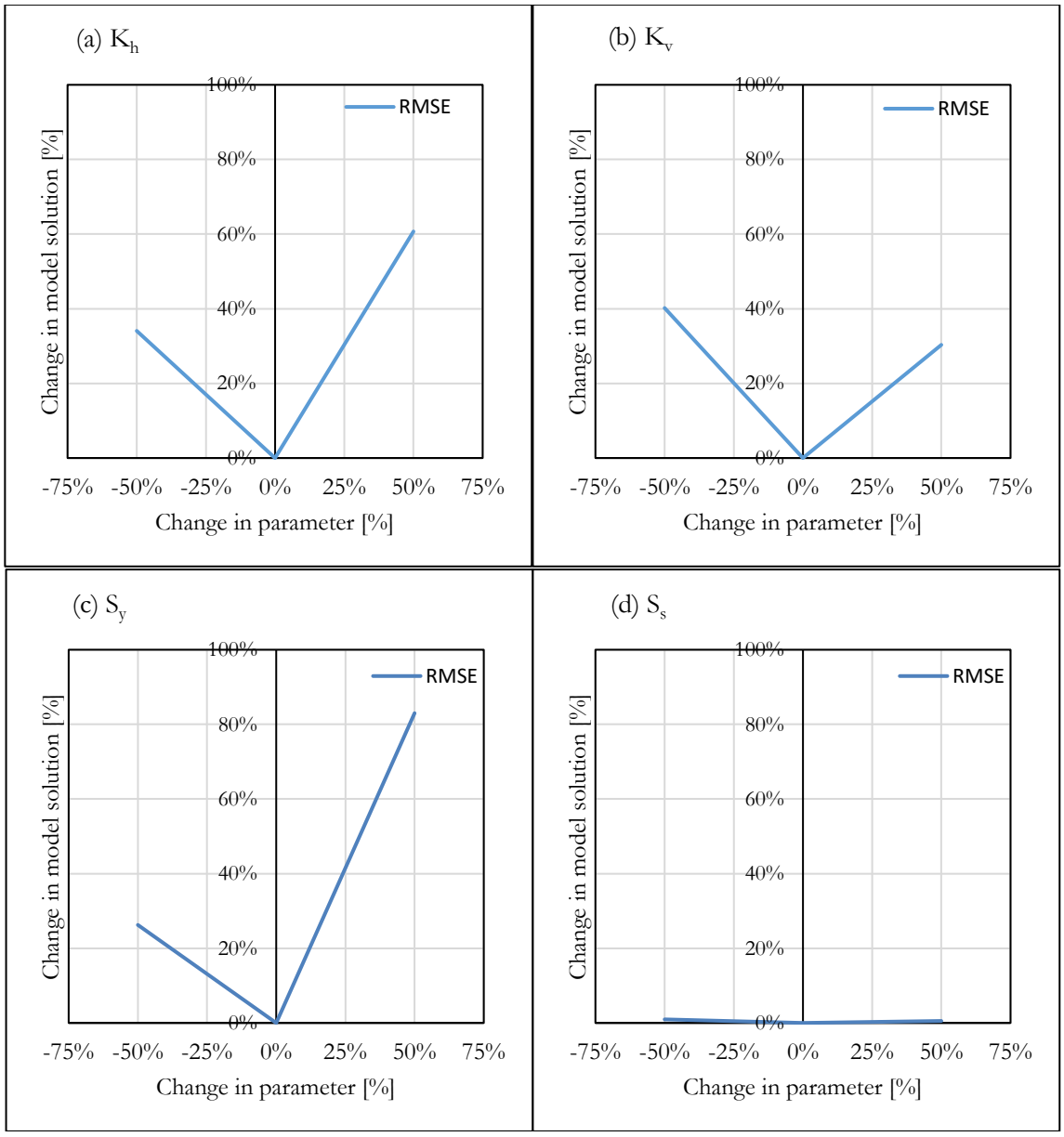

Figure 4.20 Sensitivity analysis of model parameters: (a) K_h; (b) K_v; (c) S_y; (d) S_s.

5. CONCLUSION AND RECOMMENDATION

5.1. Conclusions

In this study, an integrated hydrological model (IHM) approach was applied to study the surface groundwater interaction in the Sardon catchment representing HRS-WLE. Efforts were made for improving driving forces estimation and involving MODIS ET for calibration. In addition, the simulated soil moisture was compared with the selected satellite product. The summary is as follows.

- By applying more satellite images for driving forces estimation, the temporal vegetation developments were well captured, which lead to more representative driving forces estimation.
- The simulated ET showed a good agreement with MODIS ET as the percentage differences for all simulation years were within ±15%. Even though the model was calibrated by yearly MODIS ET for the entire catchment, the daily simulated ET also showed a good match (RMSE = 0.57 mm) with daily MODIS ET. This may indicate that yearly MODIS ET was sufficient for calibrating the model.
- The main difference between simulated ET and MODIS ET was the response to rainfall events. Simulated ET showed higher increases than MODIS ET, and this was mainly due to the significant increase of rejected infiltration evapotranspired (RI^e) resulting from heavy rainfall. This may indicate the capacity of IHM for a realistic simulation.
- In general, the simulated soil moisture showed similar pattern and magnitude compared with SSM1km product, with overall RMSE = 0.081 $m^3\ m^{-3}$ and Pearson correlation (r) = 0.65. Better agreement between simulated and satellite soil moisture was observed in dry days (RMSE = 0.057 $m^3\ m^{-3}$, r = 0.69) than in rainy days (RMSE = 0.102 $m^3\ m^{-3}$, r = 0.54).
- As a typical hard rock system with the shallow water table and low storativity, over 90% of R_g was out of the groundwater zone by Exf_{gw} and ET_g, and it revealed the difficulty in recharging the groundwater zone. A declining trend in groundwater zone storage (ΔS_g = -11.5 mm yr^{-1}) was observed over the 8-year simulation period.
- MODFLOW 6 showed great ability to simulate a complex system as Sardon catchment and provide spatio-temporal hydrological fluxes for both unsaturated and saturated zones in a realistic manner.

5.2. Recommendation

Soil moisture is a key state variable. The acceptable match between simulated soil moisture and SSM1km product may indicate the potential of a well-calibrated model for generating realistic soil moisture. More investigations can focus on soil moisture validation and its use as calibration state variable in the transient IHM.

LIST OF REFERENCES

Allen, R.G., Pereira, L.S., Raes, D., Smith, M., 1998. Crop evapotranspiration: guide- lines for computing crop water requirements. In: FAO Irrigation and Drainage Paper No. 56. FAO, Rome, Italy.

Anderson, M.P., Woessner, W.W., Hunt, R.J., 2015. Applied Groundwater Modeling, 2nd ed, Applied Groundwater Modeling. Academic Press. https://doi.org/10.1016/c2009-0-21563-7

Bakker, M., Post, V., Langevin, C.D., Hughes, J.D., White, J.T., Starn, J.J., Fienen, M.N., 2016. Scripting MODFLOW Model Development Using Python and FloPy. Groundwater 54, 733–739. https://doi.org/10.1111/GWAT.12413

Balugani, E., 2021. Partitioning of subsurface evaporation in water limited environments. University of Twente, Enschede, The Netherlands. https://doi.org/10.3990/1.9789036552127

Balugani, E., Lubczynski, M.W., Reyes-Acosta, L., van der Tol, C., Francés, A.P., Metselaar, K., 2017. Groundwater and unsaturated zone evaporation and transpiration in a semi-arid open woodland. J. Hydrol. 547, 54–66. https://doi.org/10.1016/j.jhydrol.2017.01.042

Bauer-Marschallinger, B., Freeman, V., Cao, S., Paulik, C., Schaufler, S., Stachl, T., Modanesi, S., Massari, C., Ciabatta, L., Brocca, L., Wagner, W., 2019. Toward Global Soil Moisture Monitoring with Sentinel-1: Harnessing Assets and Overcoming Obstacles. IEEE Trans. Geosci. Remote Sens. 57, 520–539. https://doi.org/10.1109/TGRS.2018.2858004

Campos, I., Villodre, J., Carrara, A., Calera, A., 2013. Remote sensing-based soil water balance to estimate Mediterranean holm oak savanna (dehesa) evapotranspiration under water stress conditions. J. Hydrol. 494, 1–9. https://doi.org/10.1016/j.jhydrol.2013.04.033

Carpintero, E., Mateos, L., Andreu, A., González-Dugo, M.P., 2020. Effect of the differences in spectral response of Mediterranean tree canopies on the estimation of evapotranspiration using vegetation index-based crop coefficients. Agric. Water Manag. 238. https://doi.org/10.1016/j.agwat.2020.106201

Daoud, M.G., 2020. Integrated hydrological model to study surface-groundwater interaction in hard rock systems using an unstructured grid approach, the Sardon Catchment, Spain. University of Twente.

Dewandel, B., Lachassagne, P., Wyns, R., Maréchal, J.C., Krishnamurthy, N.S., 2006. A generalized 3-D geological and hydrogeological conceptual model of granite aquifers controlled by single or multiphase weathering. J. Hydrol. 330, 260–284. https://doi.org/10.1016/j.jhydrol.2006.03.026

Ebrahim, G.Y., Villholth, K.G., Boulos, M., 2019. Integrated hydrogeological modelling of hard-rock semi-arid terrain: supporting sustainable agricultural groundwater use in Hout catchment, Limpopo Province, South Africa. Hydrogeol. J. 27, 965–981. https://doi.org/10.1007/s10040-019-01957-6

Francés, A.P., Lubczynski, M.W., Roy, J., Santos, F.A.M., Mahmoudzadeh Ardekani, M.R., 2014. Hydrogeophysics and remote sensing for the design of hydrogeological conceptual models in hard rocks - Sardón catchment (Spain). J. Appl. Geophys. 110, 63–81. https://doi.org/10.1016/j.jappgeo.2014.08.015

Gash, J.H.C., 1979. An analytical model of rainfall interception by forests. Q. J. R. Meteorol. Soc. 105, 43–55. https://doi.org/10.1002/qj.49710544304

Gash, J.H.C., Lloyd, C.R., Lachaud, G., 1995. Estimating sparse forest rainfall interception with an analytical model. J. Hydrol. 170, 79–86. https://doi.org/10.1016/0022-1694(95)02697-N

Glenn, E.P., Neale, C.M.U., Hunsaker, D.J., Nagler, P.L., 2011. Vegetation index-based crop coefficients to estimate evapotranspiration by remote sensing in agricultural and natural ecosystems. Hydrol. Process. 25, 4050–4062. https://doi.org/10.1002/HYP.8392

Hassan, S.M.T., Ghimire, C.P., Lubczynski, M.W., 2017. Remote sensing upscaling of interception loss from isolated oaks: Sardon catchment case study, Spain. J. Hydrol. 555, 489–505. https://doi.org/10.1016/j.jhydrol.2017.08.016

Hassan, S.M.T., Lubczynski, M.W., Niswonger, R.G., Su, Z., 2014. Surface-groundwater interactions in hard rocks in Sardon Catchment of western Spain: An integrated modeling approach. J. Hydrol. 517, 390–410. https://doi.org/10.1016/j.jhydrol.2014.05.026

Hiscock, K.M., 2005. Hydrogeology Principles and Practice. Blackwell Publishing.

Huntington, J.L., Niswonger, R.G., 2012. Role of surface-water and groundwater interactions on projected summertime streamflow in snow dominated regions: An integrated modeling approach. Water Resour. Res. 48. https://doi.org/10.1029/2012WR012319

Keim, R.F., Skaugset, A.E., Weiler, M., 2006. Storage of water on vegetation under simulated rainfall of varying intensity. Adv. Water Resour. 29, 974–986. https://doi.org/10.1016/J.ADVWATRES.2005.07.017

Lachassagne, P., Wyns, R., Dewandel, B., 2011. The fracture permeability of Hard Rock Aquifers is due neither to tectonics, nor to unloading, but to weathering processes. Terra Nov. https://doi.org/10.1111/j.1365-3121.2011.00998.x

Langevin, C.D., Hughes, J.D., Banta, E.R., Niswonger, R.G., 2017. Documentation for the MODFLOW 6 Groundwater Flow Model, Techniques and Methods. https://doi.org/10.3133/TM6A55

Lubczynski, M.W., Gurwin, J., 2005. Integration of various data sources for transient groundwater modeling with spatio-temporally variable fluxes - Sardon study case, Spain. J. Hydrol. 306, 71–96. https://doi.org/10.1016/j.jhydrol.2004.08.038

Martens, B., Miralles, D., Lievens, H., Fernández-Prieto, D., Verhoest, N.E.C., 2016. Improving terrestrial evaporation estimates over continental Australia through assimilation of SMOS soil moisture. Int. J. Appl. Earth Obs. Geoinf. 48, 146–162. https://doi.org/10.1016/J.JAG.2015.09.012

McDonald, M.G., Harbaugh, A.W., 1988. A Modular Three-Dimensional Finite-Difference Ground-Water Flow Model. U.S. Geological Techniques and Methods 6-A1.

Menzel, L., 1997. Modellierung der Evapotranspiration im System Boden-Pflanze- Atmosphäre. Zürcher Geographische Schriften 67. ETH Zürich. https://doi.org/10.3929/ethz-a-001696316

Moreno, G., Obrador, J.J., Cubera, E., Dupraz, C., 2005. Fine Root Distribution in Dehesas of Central-Western Spain. Plant Soil 2005 2771 277, 153–162. https://doi.org/10.1007/S11104-005-6805-0

Newman, B.D., Wilcox, B.P., Archer, S.R., Breshears, D.D., Dahm, C.N., Duffy, C.J., McDowell, N.G., Phillips, F.M., Scanlon, B.R., Vivoni, E.R., 2006. Ecohydrology of water-limited environments: A scientific vision. Water Resour. Res. https://doi.org/10.1029/2005WR004141

Niswonger, R.G., Panday, S., Motomu, I., 2011. MODFLOW-NWT , A Newton Formulation for MODFLOW-2005. U.S. Geological Survey Techniques and Methods 6-A37. https://doi.org/10.3133/tm6A37

Niswonger, R.G., Prudic, D.E., 2006. Documentation of the Unsaturated-Zone Flow (UZF1) Package for Modeling Unsaturated Flow Between the Land Surface and the Water Table with MODFLOW-2005. U.S. Geological Techniques and Methods 6-A19, pp. 62. https://doi.org/10.3133/tm6A19

Niswonger, R.G., Prudic, D.E., 2005. Documentation of the Streamflow-Routing (SFR2) Package to Include Unsaturated Flow Beneath Streams - A Modification to SFR1. U.S. Geological Techniques and Methods 6-A13, pp. 51. https://doi.org/10.3133/TM6A13

Peter H. Gleick, 1993. Water in Crisis: A Guide to the World's Fresh Water Resources. Oxford University Press.

Reyes-Acosta, J.L., Lubczynski, M.W., 2013. Mapping dry-season tree transpiration of an oak woodland at the catchment scale, using object-attributes derived from satellite imagery and sap flow measurements. Agric. For. Meteorol. 174–175, 184–201. https://doi.org/10.1016/j.agrformet.2013.02.012

Senay, G.B., Bohms, S., Singh, R.K., Gowda, P.H., Velpuri, N.M., Alemu, H., Verdin, J.P., 2013. Operational Evapotranspiration Mapping Using Remote Sensing and Weather Datasets: A New Parameterization for the SSEB Approach. JAWRA J. Am. Water Resour. Assoc. 49, 577–591. https://doi.org/10.1111/JAWR.12057

Singhal, B.B.S., 2008. Nature of hard rock aquifers: Hydrogeological uncertainties and ambiguities, in: Groundwater Dynamics in Hard Rock Aquifers: Sustainable Management and Optimal Monitoring Network Design. Springer Netherlands, pp. 20–39. https://doi.org/10.1007/978-1-4020-6540-8_2

UNEP, 1997. World Atlas of Desertification (2nd edition).

Vegas Galdos, F., Álvarez, C., García, A., Revilla, J.A., 2012. Estimated distributed rainfall interception using a simple conceptual model and Moderate Resolution Imaging Spectroradiometer (MODIS). J. Hydrol. 468–469, 213–228. https://doi.org/10.1016/j.jhydrol.2012.08.043

Velpuri, N.M., Senay, G.B., Singh, R.K., Bohms, S., Verdin, J.P., 2013. A comprehensive evaluation of two MODIS evapotranspiration products over the conterminous United States: Using point and gridded FLUXNET and water balance ET. Remote Sens. Environ. 139, 35–49. https://doi.org/10.1016/J.RSE.2013.07.013

Winston, R.B., 2019. ModelMuse version 4—A graphical user interface for MODFLOW 6: U.S. Geological Survey Scientific Investigations Report 2019–5036, 10 p. https://doi.org/https://doi.org/10.3133/sir20195036